

PointNSP: Autoregressive 3D Point Cloud Generation with Next-Scale Level-of-Detail Prediction

Ziqiao Meng¹ Qichao Wang² Zhiyang Dou³ Zixing Song⁴ Zhipeng Zhou²
Irwin King⁵ Peilin Zhao⁶

¹National University of Singapore ²Nanyang Technological University ³University of Hong Kong
⁴University of Cambridge ⁵The Chinese University of Hong Kong ⁶Shanghai Jiao Tong University

Abstract

Autoregressive point cloud generation has long lagged behind diffusion-based approaches in quality. The performance gap stems from the fact that autoregressive models impose an artificial ordering on inherently unordered point sets, forcing shape generation to proceed as a sequence of local predictions. This sequential bias reinforces short-range continuity but limits the model’s ability to capture long-range dependencies, thereby weakening its capacity to enforce global structural properties such as symmetry, geometric consistency, and large-scale spatial regularities. Inspired by the level-of-detail (LOD) principle in shape modeling, we propose PointNSP, a coarse-to-fine generative framework that preserves global shape structure at low resolutions and progressively refines fine-grained geometry at higher scales through a next-scale prediction paradigm. This multi-scale factorization aligns the autoregressive objective with the permutation-invariant nature of point sets, enabling rich intra-scale interactions while avoiding brittle fixed orderings. Strictly following the baseline experimental setups, empirical results on ShapeNet benchmark demonstrate that PointNSP achieves state-of-the-art (SOTA) generation quality for the first time within the autoregressive paradigm. Moreover, it surpasses strong diffusion-based baselines in parameter, training, and inference efficiency. Finally, under dense generation with 8,192 points, PointNSP’s advantages become even more pronounced, highlighting its strong scalability potential.¹

1. Introduction

Point clouds are a fundamental representation of 3D object shapes, describing each object as a collection of points in Euclidean space. They arise naturally from sensors

¹Project Homepage: <https://pointnsp.pages.dev>

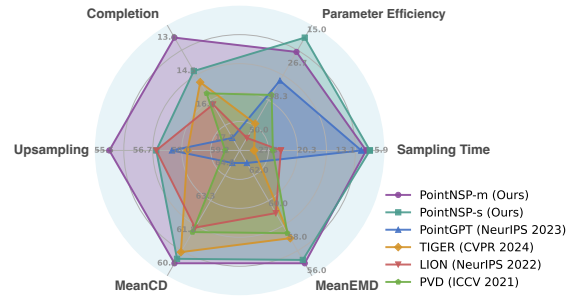


Figure 1. PointNSP achieves SoTA performance compared to recent strong baseline methods across six key evaluation metrics.

such as LiDAR and laser scanners, offering a compact yet expressive encoding of fine-grained geometric details. Developing powerful generative models for point clouds is key to uncovering the underlying distribution of 3D shapes, with broad applications in shape synthesis, reconstruction, computer-aided design, and perception for robotics and autonomous systems. However, high-fidelity point cloud generation remains challenging due to the irregular and unordered nature of point sets [38, 39, 63]. Unlike images or sequences, point clouds lack an inherent ordering—permutations do not alter the underlying shape—rendering naive order-dependent modeling strategies fundamentally misaligned with their structure.

In recent years, diffusion-based methods [46, 64, 68] have become the dominant paradigm for 3D point cloud generation, achieving strong empirical performance. However, their Markovian formulation prevents them from leveraging full historical context, often resulting in incoherent shapes. They are also computationally expensive: producing high-quality samples typically requires hundreds to thousands of denoising steps, a burden that becomes prohibitive for dense point clouds. Although advanced samplers [30, 49] can accelerate sampling, such speedups commonly degrade generation quality. By contrast, autoregressive (AR) models condition on the entire generation history, which helps enforce local smoothness and gener-

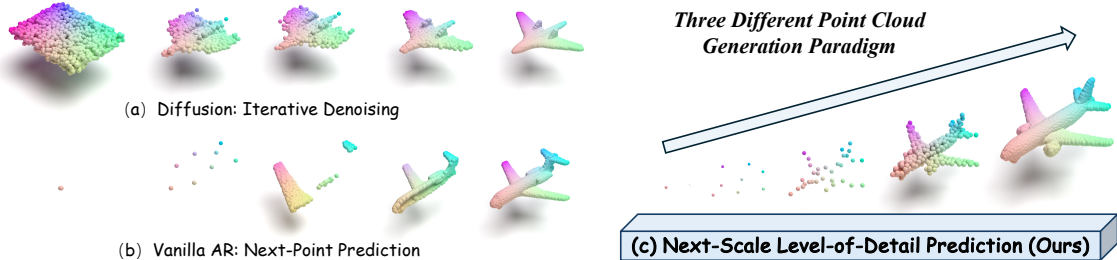


Figure 2. Three types of point cloud generative models: (a) diffusion-based methods that iteratively denoise shapes starting from Gaussian noise; (b) vanilla autoregressive (AR) methods that predict the next point by flattening the 3D shape into a sequence; and (c) our proposed *PointNSP*, which predicts next-scale level-of-detail in a coarse-to-fine manner.

ally enables faster sampling. Yet, existing AR approaches must impose an artificial ordering on the inherently unordered point set, typically by flattening it into a sequence, which adheres to a *next-point prediction* paradigm. Point Transformers [58, 59, 66] design specialized architectures for unordered point sets and explore diverse point cloud serialization strategies to improve speed, at the expense of relaxing permutation invariance. PointGrow [51] enforces a sequential order by sorting points along the z -axis. ShapeFormer [60] voxelizes point clouds and flattens codebook embeddings into sequences using a row-major order. PointVQVAE [7] projects patches onto a sphere and arranges them in a spiral sequence to establish a canonical mapping. AutoSDF [34] treats point clouds as randomly permuted sequences of latent variables, while PointGPT [4] leverages Morton code ordering to impose structure on unordered data. Although these approaches yield promising results, they still lag behind strong diffusion-based methods [33, 46, 64, 68] in generation quality. This is largely due to the restrictive unidirectional dependencies imposed by fixed sequential orders, which collapse global shape generation into local predictions and inherently violate the fundamental permutation-invariance property. This naturally raises the question: *can we achieve permutation-invariant autoregressive modeling for 3D point cloud generation?*

In this work, we introduce *PointNSP*, a novel autoregressive framework for 3D point cloud generation that preserves global permutation invariance—a key property ensuring that shapes remain independent of point ordering. *PointNSP* follows a coarse-to-fine strategy, progressively refining point clouds from global structures to fine-grained details via *next-scale prediction*. Unlike prior approaches that predict one point at a time (next-point prediction), *PointNSP* captures multiple levels of detail (LoD) [31] at each step, enabling more effective modeling of both global geometry and local structure. This design offers two key advantages. First, it avoids collapsing 3D structures by eliminating the need to flatten point clouds into 1D sequences: each step corresponds to a full 3D shape at a given LoD, ensuring structural coherence and permutation invariance.

Second, compared to diffusion-based methods, *PointNSP* establishes a more structured and efficient generation trajectory, avoiding iterative noise injection and denoising in 3D space. Together, these advances allow *PointNSP* to achieve high generation quality while maintaining strong modeling efficiency. The comparisons across different paradigms are illustrated in Figure 2.

We conduct extensive experiments on the ShapeNet benchmark to validate the effectiveness of *PointNSP* across diverse settings. In the standard single-class scenario, *PointNSP* achieves state-of-the-art (SoTA) **generation quality**, yielding the lowest average Chamfer Distance and Earth Mover’s Distance—setting a new benchmark for autoregressive modeling. Beyond quality, *PointNSP* also demonstrates substantially higher **parameter efficiency**, **training efficiency**, and **sampling speed** compared to strong diffusion-based baselines. In the more challenging many-class (55-class) generation setting, *PointNSP* maintains SoTA performance, evidencing superior cross-category generalization. Moreover, *PointNSP* significantly outperforms existing approaches on downstream tasks such as partial point cloud completion and upsampling, further highlighting the robustness and versatility of its design. Comparative results across these metrics are presented in Figure 1. When evaluated on denser point clouds with 8192 points, the advantages of *PointNSP* become even more pronounced, particularly in the aforementioned efficiency metrics, underscoring its **scalability potential**.

2. Related Works

Autoregressive Generative Modeling. The core principle of autoregressive generative models is to synthesize outputs sequentially by iteratively generating intermediate segments. This paradigm has achieved remarkable success in discrete language modeling through next-token prediction [36, 37]. Inspired by these advances, researchers have extended autoregressive modeling to other modalities, including images [8, 12, 21], speech [56, 65], and multi-modal data [52, 67]. Although these modalities are often continuous in nature, they are typically trans-

formed into discrete token representations using techniques such as VQ-VAE (VQ) [54] or residual vector quantization (RVQ) [21], with generation performed over the resulting tokens in predefined orders (e.g., raster-scan sequences). To relax the constraint of strict unidirectional dependencies, MaskGIT [3] predicts sets of randomly masked tokens at each step under the control of a scheduler. More recently, VAR [53] redefines the autoregressive paradigm by predicting the next resolution rather than the next token. Within each scale, a bidirectional transformer enables full contextual interaction among tokens, making VAR especially effective for modeling unordered data such as 3D point clouds. Note that while VAR has been applied to 3D mesh generation [22] and 2D image-conditional 3D triplane generation [6], these works differ fundamentally from ours as they operate on different 3D data structures.

Point Cloud Generation. Deep generative models have made significant strides in 3D point cloud generation. For instance, PointFlow [61] captures the latent distribution of point clouds using continuous normalizing flows [5, 14, 47]. Building on this foundation, a series of approaches—including DPM [33], ShapeGF [2], PVD [68], LION [64], TIGER [46], PDT [55]—leverage denoising diffusion probabilistic models [16, 50] to synthesize 3D point clouds through the gradual denoising of input data or latent representations in continuous space. While efforts to improve the sampling efficiency of diffusion models—such as straight flows [25, 27, 57] and ODE-based solvers [49]—have achieved acceleration, these methods often introduce trade-offs that compromise generation quality. In contrast, autoregressive models for 3D point cloud generation [4, 7, 51] have received relatively less attention, historically lagging behind diffusion-based techniques in terms of fidelity. In this work, we reformulate point cloud generation as an iterative upsampling process, establishing a connection with sparse point cloud upsampling approaches [15, 45, 62]. A comprehensive review of point cloud upsampling works is provided in the Appendix 11.

3. Method: PointNSP

3.1. Preliminaries: Autoregressive 3D Point Cloud Generation

A point cloud is represented as a set of N points $\mathbf{X} = \{\mathbf{x}_i\}_{i=1}^N$, where each point $\mathbf{x}_i \in \mathbb{R}^3$ corresponds to a 3D coordinate. Prior autoregressive approaches [4, 7, 51] mainly follow the next-point prediction paradigm:

$$p(\mathbf{x}_1, \mathbf{x}_2, \dots, \mathbf{x}_N) = \prod_{i=1}^N p(\mathbf{x}_i | \mathbf{x}_{i-1}, \dots, \mathbf{x}_2, \mathbf{x}_1). \quad (1)$$

Training Eq. 1 requires a sequential classification objective. Each point \mathbf{x}_i is first converted into a discrete integer to-

ken q_i via VQ-VAE quantization [54], and the resulting tokens are flattened into a sequence (q_1, \dots, q_N) according to a *predefined generation order*. Autoregressive modeling is then applied to this discrete sequence following the paradigm in Eq. 1. However, this approach struggles to preserve permutation invariance, since the probability distribution depends on the chosen token ordering and is not invariant to different permutations of the points. In this work, instead of predicting the next point, we propose a novel autoregressive framework that predicts the *next-scale level-of-detail (LoD)* of the point cloud \mathbf{X} , while simultaneously preserving the permutation invariance property:

$$p(\pi(\mathbf{x}_1, \dots, \mathbf{x}_N)) = p(\mathbf{x}_1, \dots, \mathbf{x}_N), \quad \forall \pi \in S_N. \quad (2)$$

In general, we construct k different LoDs of \mathbf{X} , forming a coarse-to-fine sequence of global shapes $\mathbf{X}_1, \dots, \mathbf{X}_K$, where each $\mathbf{X}_k \in \mathbb{R}^{s_k \times 3}$ represents a global shape at resolution s_k , obtained by downsampling the original \mathbf{X} . Then, *PointNSP* is designed to learn the following distribution:

$$p(\mathbf{X}_1, \mathbf{X}_2, \dots, \mathbf{X}_K) = \prod_{k=1}^K p(\mathbf{X}_k | \mathbf{X}_{k-1}, \dots, \mathbf{X}_2, \mathbf{X}_1). \quad (3)$$

The generation process bears a strong resemblance to an autoregressive upsampling procedure, governed by a sequence of upsampling rates r_1, r_2, \dots, r_{K-1} that satisfy the relation $r_{K-1} \times \dots \times r_1 \times s_1 = s_K$. We set $s_K = N$, $\mathbf{X}_K = \mathbf{X}$ to reconstruct the shape at the target full-resolution point count. Under this formulation, Eq. 3 requires learning a hierarchy of representations \mathbf{X}_k across multiple LoD information. These representations progressively encode more global and semantically coherent structural information than the next-point prediction in Eq. 1.

3.2. Multi-Scale LoD Representation

Sampling LoD Sequence. To construct the LoD sequence $(\mathbf{X}_1, \dots, \mathbf{X}_K)$ for each sample \mathbf{X} , three key considerations must be addressed. First, the sampling operation should preserve the permutation invariance property of point clouds, ensuring that the resulting LoD sequence remains independent of the input point ordering in \mathbf{X} . Second, the sampling strategy should aim for *comprehensive spatial coverage* at each LoD, reflecting the existence of an underlying continuous surface that the 3D shape represents. To this end, we adopt the Farthest Point Sampling (FPS) [11] algorithm to construct the LoD sequence. The point selection mechanism in FPS relies exclusively on spatial geometry—specifically, pairwise Euclidean distances—rather than the ordering of points within the input set, thereby preserving permutation invariance. Moreover, the inherent stochasticity introduced by the random initialization of the starting point enables diverse subsets \mathbf{X}_k to be sampled at each scale k across different training epochs,

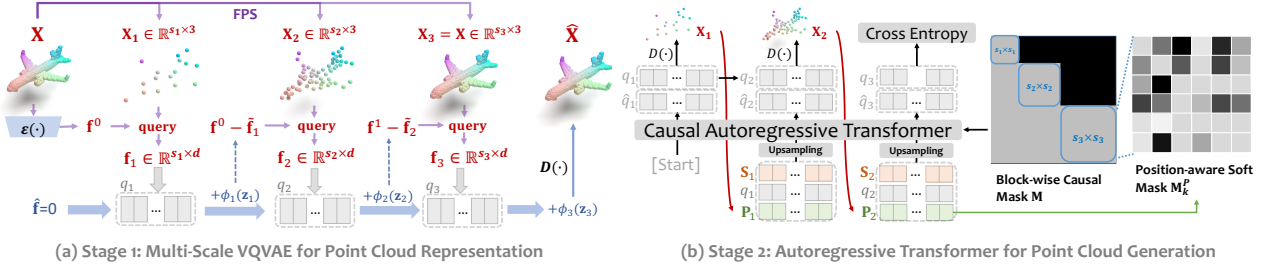


Figure 3. (a) Illustration of training a multi-scale VQVAE in a residual manner for point cloud representation across scales s_1 to s_3 , resulting in a multi-scale token sequence $Q = (q_1, \dots, q_3)$; (b) Illustration of training a causal transformer with intermediate shape decoding, scale token upsampling ($s_1 \rightarrow s_2$ and $s_2 \rightarrow s_3$), position-aware soft masks M_k^P , and block-wise causal masks M .

thereby enhancing the diversity and representational robustness of the generated LoD sequences.

Multi-Scale Feature Extraction. Rather than directly learning tokenizers from the sampled point clouds in the 3D coordinate space, we learn their corresponding quantized representations within the latent feature space defined by the LoD sequence. To obtain latent features $\mathbf{f}^0 \in \mathbb{R}^{N \times d}$ from the point cloud \mathbf{X} , any permutation-equivariant network $\text{NN}(\cdot)$ is applicable: the per-point features reorder consistently with any permutation of the input points, i.e., $\pi(\text{NN}(\mathbf{x}_1, \dots, \mathbf{x}_N)) = \text{NN}(\pi(\mathbf{x}_1, \dots, \mathbf{x}_N))$ for any permutation π . Therefore, permutation-equivariant architectures such as PointNet [38], PointNet++ [39], PointNeXt [41] and PVCNN [28] are all applicable. To encourage each scale to capture *complementary information* rather than redundantly encoding features already represented at coarser levels, we extract latent features $\mathbf{f}_k \in \mathbb{R}^{s_k \times d}$ in a residual fashion:

$$\mathbf{f}_k = \text{query}(\mathbf{f}^{k-2} - \tilde{\mathbf{f}}_{k-1}, \mathbf{X}_k), \mathbf{f}_1 = \text{query}(\mathbf{f}^0, \mathbf{X}_1). \quad (4)$$

Here, $\tilde{\mathbf{f}}_{k-1}$ represents the feature contribution from the learned tokenizers at scale $k-1$, while $\text{query}(\cdot)$ retrieves latent features according to the index correspondence between the sampled subset \mathbf{X}_k and the original point set \mathbf{X} , ensuring consistent alignment across scales. This produces a sequence of LoD latent features $(\mathbf{f}_1, \dots, \mathbf{f}_K)$.

Multi-Scale VQVAE Tokenizer. For each scale k , we learn tokenizers for latent feature \mathbf{f}_k through quantization \mathcal{Q} into discrete tokens $q_k = (q_k^1, q_k^2, \dots, q_k^{s_k}) = \mathcal{Q}(\mathbf{f}_k) \in [V]$, where $[V]$ denotes a sequence of entries corresponding to indices in a learnable codebook $Z \in \mathbb{R}^{V \times d}$ containing V vectors. Note that this codebook Z is shared across all scales for efficient utilization. Each token q_k^i indexes the nearest codebook embedding $\mathbf{z}_v \in \mathbb{R}^d$ to the corresponding latent feature $\mathbf{f}_k[i] \in \mathbb{R}^d$: $q_k^i = \arg \min_{v \in [V]} \|\mathbf{z}_v - \mathbf{f}_k[i]\|_2$. This produces scale-wise token sequence $Q = (q_1, \dots, q_K)$ along with their corresponding embeddings $(\mathbf{z}_1 \in \mathbb{R}^{s_1 \times d}, \dots, \mathbf{z}_K \in \mathbb{R}^{s_K \times d})$, forming a hierarchical discrete representation aligned with the LoD sequence. For

each scale k , the feature contribution $\tilde{\mathbf{f}}_k$ produced by the scale-specific tokenizers q_k is then given by:

$$\tilde{\mathbf{f}}_k = \phi_k(\text{upsampling}(\mathbf{z}_k, s_K)), \mathbf{z}_k = \text{lookup}(Z, q_k), \quad (5)$$

where $\phi_k(\cdot) : \mathbb{R}^{N \times d} \rightarrow \mathbb{R}^{N \times d}$ is a permutation-equivariant network that refines the latent embeddings, and $\text{upsampling}(\cdot, s_K)$ increases the resolution of the latent $\mathbf{z}_k \in \mathbb{R}^{s_k \times d}$ to the highest resolution $s_K \times d$.

Upsampling & Reconstruction. The partial sum of all feature contributions is computed as $\hat{\mathbf{f}} = \sum_{k=1}^K \tilde{\mathbf{f}}_k$, and the final predicted 3D shape $\hat{\mathbf{X}}$ is reconstructed via a simple MLP decoder $D(\cdot) : \mathbb{R}^{N \times d} \rightarrow \mathbb{R}^{N \times 3}$: $\hat{\mathbf{X}} = D(\hat{\mathbf{f}})$. This formulation demonstrates that $\hat{\mathbf{X}}$ is obtained by aggregating information across all scales of the LoD hierarchy, effectively combining coarse and fine features to generate the final 3D reconstruction. The upsampling in Eq. 5 follows a PU-Net [62]-inspired procedure, which consists of duplication and reshaping operations:

$$\mathbf{z}_k(s_k \times d) \xrightarrow{\text{duplicate}} \mathbf{z}_k(s_k \times r \times d) \xrightarrow{\text{reshape}} \mathbf{z}_k((s_k \cdot r) \times d), \quad (6)$$

where $\mathbf{z}_k \in \mathbb{R}^{(s_k \cdot r) \times d} = \mathbf{z}_K \in \mathbb{R}^{s_K \times d}$ denotes the upsampled representation at the largest scale s_K , with upsampling rate $r = \frac{s_K}{s_k}$ specified in advance. This operation densifies points by arbitrary factors while preserving the permutation-equivariance of the latent features. The reconstruction loss is defined as:

$$\mathcal{L}_{\text{recon}} = \mathcal{L}_{\text{CD}}(\mathbf{X}, \hat{\mathbf{X}}) + \mathcal{L}_{\text{EMD}}(\mathbf{X}, \hat{\mathbf{X}}) + \sum_{k=1}^K \|\mathbf{f}_k - \text{sg}(\mathbf{z}_k)\|_2^2, \quad (7)$$

where \mathcal{L}_{CD} and \mathcal{L}_{EMD} denote the Chamfer Distance and Earth Mover’s Distance losses, commonly used to evaluate point cloud similarity from complementary perspectives. The stop-gradient operation $\text{sg}[\cdot]$ ensures that the latent features \mathbf{f}_k used for reconstruction remain consistent with the quantized latent vectors \mathbf{z}_k . The above process is described in Algorithm 1 and 2 and Figure 3 (a).

Algorithm 1 Multi-scale VQVAE encoder

- 1: **Input:** 3D point cloud $\mathbf{X} = \{\mathbf{x}_i\}_{i=1}^N$.
- 2: **Hyperparameters:** # scales $\{s_k\}_{k=1}^K$.
- 3: $\mathbf{f}^0 = \mathcal{E}(\mathbf{X})$, $Q = []$;
- 4: **for** $k = 1, \dots, K$ **do**
- 5: $\mathbf{X}_k = \text{FPS}(\mathbf{X}, s_k)$
- 6: $q_k = \mathcal{Q}(\mathbf{f}_k)$, $\mathbf{f}_k = \text{query}(\mathbf{f}^k, \mathbf{X}_k)$
- 7: $Q = \text{queue_push}(Q, q_k)$
- 8: $\mathbf{z}_k = \text{lookup}(Z, q_k)$
- 9: $\mathbf{z}_k = \text{upsampling}(\mathbf{z}_k, s_K)$
- 10: $\mathbf{f}^k = \mathbf{f}^{k-1} - \phi_k(\mathbf{z}_k)$
- 11: **end for**
- 12: **Return:** token sequence $Q = (q_1, \dots, q_K)$.

Algorithm 2 Multi-scale VQVAE decoder

- 1: **Input:** token sequence $Q = (q_1, \dots, q_K)$.
- 2: **Hyperparameters:** # scales $\{s_k\}_{k=1}^K$.
- 3: $\hat{\mathbf{f}} = 0$
- 4: **for** $k = 1, \dots, K$ **do**
- 5: $q_k = \text{queue_pop}(Q)$
- 6: $\mathbf{z}_k = \text{lookup}(Z, q_k)$
- 7: $\mathbf{z}_k = \text{upsampling}(\mathbf{z}_k, s_K)$
- 8: $\hat{\mathbf{f}} = \hat{\mathbf{f}} + \phi_k(\mathbf{z}_k)$
- 9: **end for**
- 10: $\hat{\mathbf{X}} = \mathcal{D}(\hat{\mathbf{f}})$
- 11: **Return:** reconstructed point cloud $\hat{\mathbf{X}}$

3.3. Autoregressive Transformer for Next-Scale LoD Prediction

The next step is to train an autoregressive transformer on the input multi-scale token sequence $Q = ([\text{start}], q_1, \dots, q_{K-1})$ to predict (q_1, \dots, q_K) . Owing to the strong local-geometry inductive bias in 3D structures, a standard causal transformer struggles to capture both intra-scale and inter-scale dependencies efficiently. Therefore, it is necessary to incorporate geometric information into the transformer design, which poses additional challenges due to the unordered nature of point clouds.

Inter-Scale Interaction Modeling. Inter-scale interactions across input scales (q_1, \dots, q_{K-1}) are critical for the model to capture dependencies between levels of detail and to generate each subsequent LoD conditioned on the preceding ones. We follow a key principle: *Tokens at scale q_k are permitted to attend only to tokens from preceding scales q_1, \dots, q_{k-1} . Within each scale, however, all tokens $q_k = (q_k^1, \dots, q_k^{s_k})$ are allowed to fully attend to one another, ensuring that the model interprets them as complete shapes at the corresponding resolution.* To enforce this constraint, we construct a causal mask $\mathbf{M} \in$

$\mathbb{R}^{(s_1+\dots+s_K) \times (s_1+\dots+s_K)}$ as a block-diagonal matrix, where each diagonal block \mathbf{M}_k of size $s_k \times s_k$ is fully unmasked: $\mathbf{M} = \text{diag}[\mathbf{M}_1, \mathbf{M}_2, \dots, \mathbf{M}_K]$. This design allows bidirectional attention within each scale while maintaining a lower-triangular dependency structure across scales, thereby preventing information leakage from future scale tokens. To further distinguish scales, each token is assigned a scale embedding $\mathbf{s}_k^i \in \mathbb{R}^d$, implemented as a one-hot embedding over K scales and shared among tokens within the same scale. Algorithmic details are explained in the Appendix 7.

Intra-Scale Interaction Modeling. Since the intra-scale bidirectional transformer does not inherently encode positional information, stacking multiple transformer layers can dilute the relative positional signals among tokens. To mitigate this issue, we first add positional encodings to the token embeddings after each transformer layer. In addition, we augment \mathbf{M}_k with a position-aware soft masking matrix $\mathbf{M}_k^p \in \mathbb{R}^{s_k \times s_k}$, which is derived from the coordinate-based absolute positional embedding matrix $\mathbf{P}_k \in \mathbb{R}^{s_k \times d}$:

$$\mathbf{M}_k^p = \text{Softmax}((\mathbf{P}_k \mathbf{W}_p)(\mathbf{P}_k \mathbf{W}_p)^T), \quad \mathbf{W}_p \in \mathbb{R}^{d \times d}. \quad (8)$$

\mathbf{M}_k^p is a symmetric matrix, where each entry $\mathbf{M}_k^p[i, j] \in (0, 1)$ encodes the soft relative position information between points i and j . This raises a key question: *how can we derive the positional embedding \mathbf{P}_k for each scale when no explicit 3D geometry is available at this stage?* Our solution is an intermediate-structure decoding strategy. Specifically, we apply the decoder $D(\cdot)$ to reconstruct the intermediate structure \mathbf{X}_k using all ground-truth tokens up to step k :

$$\mathbf{X}_k = D\left(\sum_{m=1}^k \phi_m(\text{upsampling}(\mathbf{z}_m, s_m))\right), \quad (9)$$

where $(\mathbf{z}_1, \dots, \mathbf{z}_k) = \text{lookup}(Z, (q_1, \dots, q_k))$, $\mathbf{X}_k \in \mathbb{R}^{s_k \times 3}$ provides the coordinate information used to compute the positional embedding \mathbf{P}_k . \mathbf{P}_k is derived as an absolute positional encoding based on the 3D coordinates \mathbf{X}_k using trigonometric functions (e.g. \sin and \cos). During inference, the predicted token \hat{q}_k is used to obtain $\hat{\mathbf{z}}_k$ in Eq. 9, rather than the ground-truth token q_k , which is not available at test time. The detailed derivation of \mathbf{P} is provided in the Appendix 7. Note that any positional encoding based on token indices should not be applied, as it would violate the permutation equivariance property.

The prediction of each token \hat{q}_k^i is evaluated using the cross-entropy (CE) loss $\mathcal{L}_k^i = \text{CE}(\hat{q}_k^i, q_k^i)$. We first compute intra-scale loss $\mathcal{L}_k = \frac{1}{s_k} \sum_{i=1}^{s_k} \mathcal{L}_k^i$ and then compute inter-scale loss $\mathcal{L}_{\text{total}} = \frac{1}{K} \sum_{k=1}^K \mathcal{L}_k$. The second stage training architecture is illustrated in Figure 3 (b). We provide a theoretical analysis of the permutation invariance of *PointNSP*'s distribution modeling in Appendix 6.

Model	Generative Model	Airplane		Chair		Car		Mean CD ↓	Mean EMD ↓
		CD ↓	EMD ↓	CD ↓	EMD ↓	CD ↓	EMD ↓		
ShapeGF [2]	Diffusion	80.00	76.17	68.96	65.48	63.20	56.53	70.72	66.06
DPM [33]	Diffusion	76.42	86.91	60.05	74.77	68.89	79.97	68.45	80.55
PVD [68]	Diffusion	73.82	64.81	56.26	53.32	54.55	53.83	61.54	57.32
LION [64]	Diffusion	72.99	64.21	55.67	53.82	53.47	53.21	61.75	57.59
TIGER [46]	Diffusion	73.02	64.10	55.15	53.18	53.21	53.95	60.46	57.08
PointGrow [51]	Autoregressive	82.20	78.54	63.14	61.87	67.56	65.89	70.96	68.77
CanonicalVAE [7]	Autoregressive	80.15	76.27	62.78	61.05	63.23	61.56	68.72	66.29
PointGPT [4]	Autoregressive	74.85	65.61	57.24	55.01	55.91	54.24	63.44	62.24
<i>PointNSP-s (ours)</i>	Autoregressive	<u>72.92</u>	<u>63.98</u>	<u>54.89</u>	<u>53.02</u>	<u>52.86</u>	<u>52.07</u>	<u>60.22</u>	<u>56.36</u>
<i>PointNSP-m (ours)</i>	Autoregressive	72.24	63.69	54.54	52.85	52.17	51.85	59.65	56.13
LION	Diffusion	67.41	61.23	<u>53.70</u>	52.34	<u>53.41</u>	51.14	<u>58.17</u>	54.90
TIGER	Diffusion	67.21	56.26	54.32	51.71	54.12	50.24	58.55	52.74
<i>PointNSP-s (ours)</i>	Autoregressive	<u>67.15</u>	<u>56.12</u>	54.22	<u>51.19</u>	53.98	<u>50.15</u>	58.45	<u>52.49</u>
<i>PointNSP-m (ours)</i>	Autoregressive	66.98	56.05	54.01	53.76	53.12	50.09	58.04	52.30

Table 1. Performance under the standard 2048-point setup on ShapeNet is reported for two dataset splits: the top corresponds to the conventional random split, and the bottom corresponds to the LION split [64]. The best results are highlighted in bold with a green bar, and the second-best results are underlined.

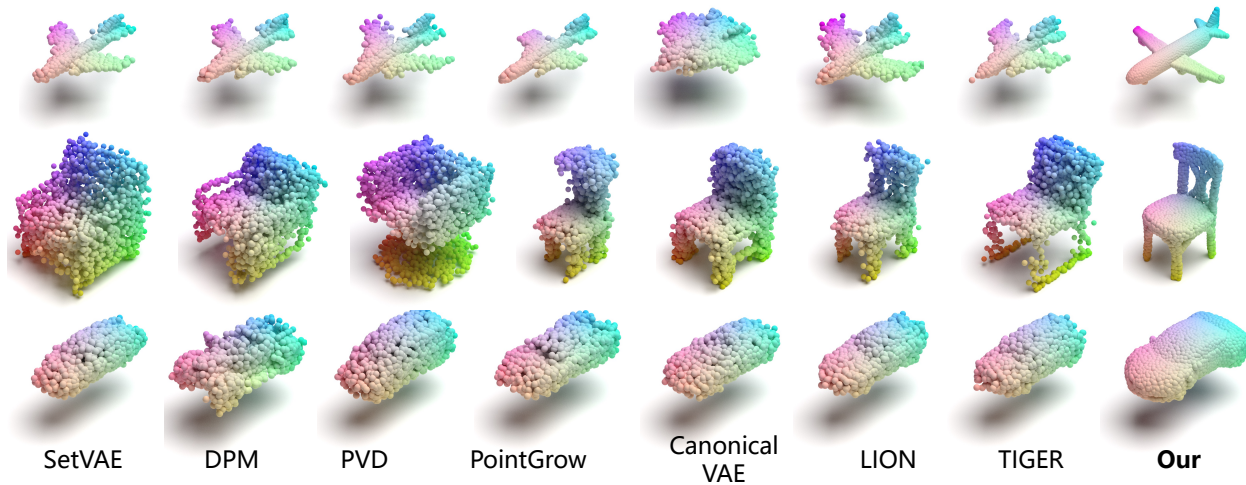


Figure 4. Visualization of generation results compared with baseline models. *PointNSP* produces high-quality and diverse 3D point clouds.

4. Experiments

4.1. Experimental Setup

Datasets & Metrics. In line with prior studies, we adopt ShapeNetv2, pre-processed by PointFlow [61], as our primary dataset. Each shape is globally normalized and uniformly sampled to 2048 points (standard setting). Experiments under this setting are conducted on two data splits: the standard random split and the LION split [46, 64]. We further evaluate a dense generation setting with 8192 points (dense setting). Following established benchmarks [64, 68], we use the 1-nearest neighbor (1-NN) accuracy [29] as our primary evaluation metric, which effectively captures both the quality and diversity of generated point clouds—a score

near 50% indicates strong performance [61]. The 1-NN distance matrix is computed using two widely adopted distance measures: Chamfer Distance (CD) and Earth Mover’s Distance (EMD). We also report mean CD and mean EMD, averaged across all object categories. To assess efficiency, we record the total training time in GPU hours and report both inference time and parameter count.

4.2. Single-Class Generation: Standard & Dense

Results. To comprehensively assess the performance of *PointNSP*, we compare it with several strong baseline models. Specifically, we include SoTA diffusion-based approaches—ShapeGF [2], DPM [33], PVD [68], LION [64], and TIGER [46]—as well as leading autoregressive models,

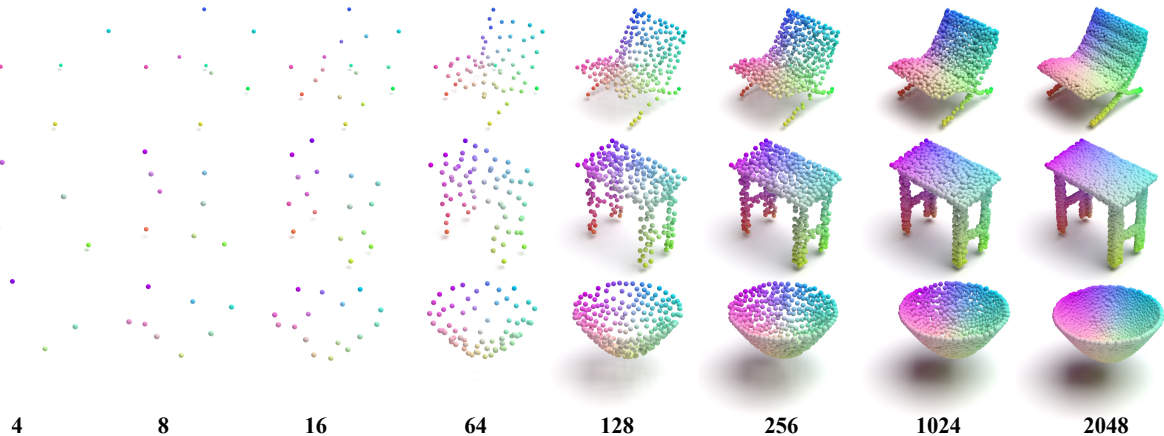


Figure 5. Visualization of multi-scale point clouds during the *PointNSP* generation process as the scale K increases.

Model	Dense Point Cloud Generation (8192 pts)						Many-Class Generation (55-Class)					
	Airplane		Chair		Car		Airplane		Chair		Car	
	CD ↓	EMD ↓	CD ↓	EMD ↓	CD ↓	EMD ↓	CD ↓	EMD ↓	CD ↓	EMD ↓	CD ↓	EMD ↓
PVD	69.77	69.98	52.56	51.33	54.19	46.55	97.53	99.88	88.37	96.37	89.77	94.89
TIGER	68.48	60.24	51.87	51.85	53.78	44.12	83.54	81.55	57.34	61.45	65.79	57.24
PointGPT	69.29	61.56	52.43	52.09	54.97	45.20	94.94	91.73	71.83	79.00	89.35	87.22
LION	68.95	60.38	53.76	53.45	54.98	44.67	86.30	77.04	66.50	63.85	64.52	54.21
<i>PointNSP-s (ours)</i>	67.84	58.25	51.26	51.81	52.40	43.76	78.95	68.84	58.79	55.10	59.97	52.89
<i>PointNSP-m (ours)</i>	66.63	55.29	50.98	50.45	52.12	43.05	75.42	66.54	56.03	52.22	57.95	49.55

Table 2. Comparison of dense point cloud generation (left) and many-class generation (right). CD and EMD metrics (↓) are reported.

Quality ↓	Model	2048 pts		8192 pts		Param ↓
		Training ↓	Sampling ↓	Training ↓	Sampling ↓	
6	PointGPT	185	5.32	296	10.56	46
5	PVD	142	29.9	201	58.1	45
4	LION	550	31.2	610	59.5	60
3	TIGER	164	23.6	320	42.1	55
2	<i>PointNSP-s (ours)</i>	125	3.21	175	4.54	22
1	<i>PointNSP-m (ours)</i>	178	3.59	190	5.48	32

Table 3. Training time (in GPU hours, averaged over three categories), sampling time (in seconds, averaged over samples), and model size (in millions of parameters). Ranked by generation quality on 2048 and 8192 settings.

including PointGrow [51], CanonicalVAE [7], and PointGPT [4]. We report results for two variants of our model, *PointNSP-s* and *PointNSP-m*, corresponding to small and medium parameter configurations, respectively. *Note that we only compare against models with publicly available implementations.* **Quality.** As shown in Table 1, *PointNSP* consistently surpasses all baseline methods on both the conventional and LION data splits under the standard 2048-point setting, establishing new SoTA generation quality. Notably, even the lightweight *PointNSP-s* achieves highly competitive results. Under the dense 8192-point setting, Table 2 (Left) further demonstrates that *PointNSP* outperforms strong baselines by an increasingly larger margin. **Efficiency.** Table 3 reports the training time, sampling

time, and model size for several strong baseline models from Table 1, including PVD, LION, TIGER, and PointGPT. Among these, *PointNSP-s* achieves the shortest training time, fastest sampling speed, and highest parameter efficiency, while still delivering competitive performance. *PointNSP-m* attains state-of-the-art generation quality with the second-best efficiency, slightly trailing its lighter counterpart. Under the dense 8192-point setting, *PointNSP-m* requires only about half as many parameters as leading diffusion-based models while maintaining superior performance. Collectively, these results highlight the strong scalability potential of *PointNSP*.

4.3. Many-Class Unconditional Generation

Beyond the Single-Class generation setting, we further evaluate our model on the more challenging Many-Class generation task introduced by LION [64], aiming to assess its ability to generalize across diverse object categories. Specifically, we train *PointNSP* and selected strong baseline models without using class conditioning over 55 distinct categories from ShapeNet. This poses a challenge for the model to capture multi-modal and structurally complex geometric patterns across categories. As shown in Table 2 (Right), *PointNSP* significantly outperforms all strong base-

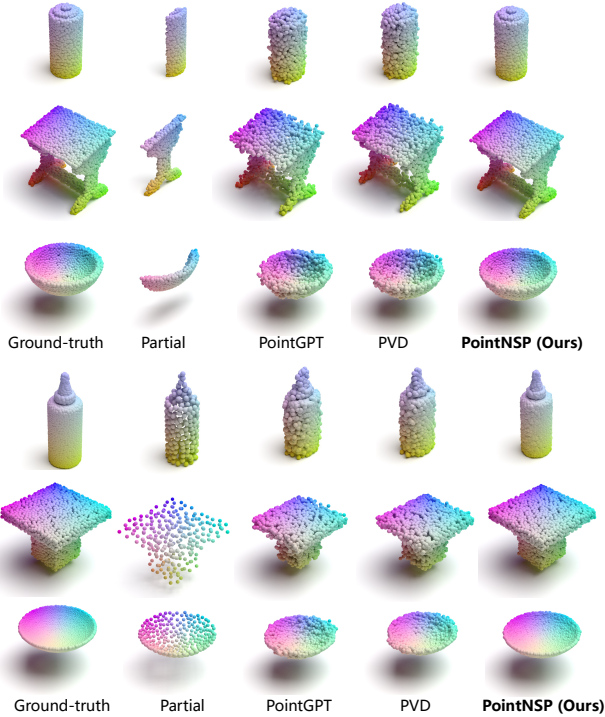


Figure 6. (Left) Visualizations of point cloud completion results. (Right) Visualizations of point cloud upsampling results.

lines. We provide visualizations of diverse shape classes in Appendix 10.

4.4. Point Cloud Completion & Upsampling

We evaluate *PointNSP* on two key downstream tasks: point cloud completion and upsampling. For completion, we follow the experimental setup of PVD [68]. For upsampling, we use a factor of $r = 2$, increasing the input point clouds from 1024 to 2048 points. As shown in Table 5, *PointNSP* consistently achieves the best performance on point cloud completion. For the upsampling task, it outperforms all selected baselines across both metrics, highlighting its effectiveness on diverse downstream applications and its potential as a foundation model. Visualization results for these two tasks are presented in Figure 6 and Appendix 10.

4.5. Ablation and Analysis

We conduct comprehensive ablation studies to assess the impact of various architectural components and training strategies. First, we compare two upsampling strategies: *voxel-based representations* and *PU-Net*. Our experiments show that *PU-Net* consistently outperforms *voxel-based upsampling*, owing to its permutation-equivariant design. Second, we evaluate the effectiveness of the *position-aware masking strategy*, which significantly boosts model performance. Third, we analyze the contribution of each embed-

Position Mask	Upsampling		FPS Stochasticity	TE	Mean CD ↓	Mean EMD ↓
	Voxel	PU-Net				
				SE	64.25	60.53
✓		✓		SE	63.86	59.95
✓		✓		SE+A-PE	62.19	58.23
✓	✓	✓		SE+A-PE	63.05	58.47
✓		✓		L-PE	63.22	59.71
✓		✓		A-PE	62.12	60.02
✓		✓	✓	A-PE	61.28	57.32
✓		✓	✓	SE+L-PE	60.62	57.34
✓		✓	✓	SE+A-PE	59.65	56.13

Table 4. Training time (in GPU hours, averaged over three categories), sampling time (in seconds, averaged over samples), and model size (in millions of parameters). Ranked by generation quality on 2048 and 8192 settings.

Category	Point Cloud Completion			Point Cloud Upsampling		
	Model	CD ↓	EMD ↓	Model	CD ↓	EMD ↓
Airplane	SoftFlow	40.42	11.98	PVD	73.56	71.65
	PointFlow	40.30	11.80	TIGER	71.65	59.94
	DPF-Net	52.79	11.05	PointGPT	72.11	60.12
	PVD	44.15	10.30	LION	70.41	59.65
	PointNSP-m (ours)	40.12	10.08	PointNSP-m (ours)	68.89	58.86
Chair	SoftFlow	27.86	32.95	PVD	53.81	64.61
	PointFlow	27.07	36.49	TIGER	52.80	52.98
	DPF-Net	27.63	33.20	PointGPT	53.75	53.21
	PVD	32.11	29.39	LION	53.98	54.33
	PointNSP-m (ours)	27.02	28.78	PointNSP-m (ours)	52.04	51.03
Car	SoftFlow	18.50	27.89	PVD	58.95	48.43
	PointFlow	18.03	28.51	PointGPT	57.26	47.85
	DPF-Net	13.96	23.18	TIGER	57.90	48.01
	PVD	17.74	21.46	LION	57.14	47.56
	PointNSP-m (ours)	13.84	20.68	PointNSP-m (ours)	55.85	46.74

Table 5. Comparison on partial shape completion (left) and point cloud upsampling task (right).

ding in the token embedding layer, with results highlighting the notable impact of the scale embedding. We also compare *learnable positional encoding (L-PE)* with *absolute PE (A-PE)*, finding that *A-PE* yields better performance. Finally, we examine the impact of *FPS stochasticity*, which stems from the inherent randomness of the *FPS* algorithm. Compared to a variant with a fixed initialization that yields deterministic downsampling, our results show that incorporating *FPS stochasticity* consistently improves model generalization. These findings are summarized in Table 4, with additional ablations—such as varying the number of scales—presented in Appendix 8.

5. Conclusions

In this work, we introduce *PointNSP*, a novel autoregressive framework for high-quality 3D point cloud generation. Unlike previous approaches, *PointNSP* employs a coarse-to-fine strategy that captures the multi-scale level of detail (LoD) of 3D shapes while preserving global structural coherence, rather than decomposing generation into local predictions. Our method consistently surpasses existing point cloud generative models in quality, while achieving substantial gains in parameter efficiency, training efficiency, and inference speed. Looking ahead, we aim to extend *PointNSP* toward foundation-scale models trained on large-scale 3D datasets as a promising future direction.

References

- [1] Panos Achlioptas, Olga Diamanti, Ioannis Mitliagkas, and Leonidas J. Guibas. Learning representations and generative models for 3d point clouds. In *Proceedings of the 35th International Conference on Machine Learning, ICML 2018, Stockholmsmässan, Stockholm, Sweden, July 10-15, 2018*, pages 40–49. PMLR, 2018. 3, 4
- [2] Ruojin Cai, Guandao Yang, Hadar Averbuch-Elor, Zekun Hao, Serge J. Belongie, Noah Snavely, and Bharath Hariharan. Learning gradient fields for shape generation. In *Computer Vision - ECCV 2020 - 16th European Conference, Glasgow, UK, August 23-28, 2020, Proceedings, Part III*, pages 364–381. Springer, 2020. 3, 6, 4
- [3] Huiwen Chang, Han Zhang, Lu Jiang, Ce Liu, and William T. Freeman. Maskgit: Masked generative image transformer. In *IEEE/CVF Conference on Computer Vision and Pattern Recognition, CVPR 2022, New Orleans, LA, USA, June 18-24, 2022*, pages 11305–11315. IEEE, 2022. 3
- [4] Guangyan Chen, Meiling Wang, Yi Yang, Kai Yu, Li Yuan, and Yufeng Yue. Pointgpt: Auto-regressively generative pre-training from point clouds. In *Advances in Neural Information Processing Systems 36: Annual Conference on Neural Information Processing Systems 2023, NeurIPS 2023, New Orleans, LA, USA, December 10 - 16, 2023*, 2023. 2, 3, 6, 7, 4
- [5] Tian Qi Chen, Yulia Rubanova, Jesse Bettencourt, and David Duvenaud. Neural ordinary differential equations. In *Advances in Neural Information Processing Systems 31: Annual Conference on Neural Information Processing Systems 2018, NeurIPS 2018, December 3-8, 2018, Montréal, Canada*, pages 6572–6583, 2018. 3
- [6] Yongwei Chen, Yushi Lan, Shangchen Zhou, Tengfei Wang, and Xingang Pan. SAR3D: autoregressive 3d object generation and understanding via multi-scale 3d VQVAE. In *IEEE/CVF Conference on Computer Vision and Pattern Recognition, CVPR 2025, Nashville, TN, USA, June 11-15, 2025*, pages 28371–28382. Computer Vision Foundation / IEEE, 2025. 3
- [7] An-Chieh Cheng, Xueting Li, Sifei Liu, Min Sun, and Ming-Hsuan Yang. Autoregressive 3d shape generation via canonical mapping. In *Computer Vision - ECCV 2022 - 17th European Conference, Tel Aviv, Israel, October 23-27, 2022, Proceedings, Part III*, pages 89–104. Springer, 2022. 2, 3, 6, 7, 4
- [8] Alexey Dosovitskiy, Lucas Beyer, Alexander Kolesnikov, Dirk Weissenborn, Xiaohua Zhai, Thomas Unterthiner, Mostafa Dehghani, Matthias Minderer, Georg Heigold, Sylvain Gelly, Jakob Uszkoreit, and Neil Houlsby. An image is worth 16x16 words: Transformers for image recognition at scale. In *9th International Conference on Learning Representations, ICLR 2021, Virtual Event, Austria, May 3-7, 2021*. OpenReview.net, 2021. 2
- [9] Hang Du, Xuejun Yan, Jingjing Wang, Di Xie, and Shiliang Pu. Point cloud upsampling via cascaded refinement network. In *Computer Vision - ACCV 2022 - 16th Asian Conference on Computer Vision, Macao, China, December 4-8, 2022, Proceedings, Part I*, pages 106–122. Springer, 2022. 3
- [10] Abhimanyu Dubey, Abhinav Jauhri, Abhinav Pandey, Abhishek Kadian, Ahmad Al-Dahle, Aiesha Letman, Akhil Mathur, Alan Schelten, Amy Yang, Angela Fan, Anirudh Goyal, Anthony Hartshorn, Aobo Yang, Archi Mitra, Archie Sravankumar, Artem Korenev, Arthur Hinsvark, Arun Rao, Aston Zhang, Aurélien Rodriguez, Austen Gregerson, Ava Spataru, Baptiste Rozière, Bethany Biron, Binh Tang, Bobbie Chern, Charlotte Caucheteux, Chaya Nayak, Chloe Bi, Chris Marra, Chris McConnell, Christian Keller, Christophe Touret, Chunyang Wu, Corinne Wong, Cristian Canton Ferrer, Cyrus Nikolaidis, Damien Allonsius, Daniel Song, Danielle Pintz, Danny Livshits, David Esiobu, Dhruv Choudhary, Dhruv Mahajan, Diego Garcia-Olano, Diego Perino, Dieuwke Hupkes, Egor Lakomkin, Ehab AlBadawy, Elina Lobanova, Emily Dinan, Eric Michael Smith, Filip Radenovic, Frank Zhang, Gabriel Synnaeve, Gabrielle Lee, Georgia Lewis Anderson, Graeme Nail, Grégoire Mialon, Guan Pang, Guillem Cucurell, Hailey Nguyen, Hannah Korevaar, Hu Xu, Hugo Touvron, Iliyan Zarov, Imanol Arrieta Ibarra, Isabel M. Kloumann, Ishan Misra, Ivan Evtimov, Jade Copet, Jaewon Lee, Jan Geffert, Jana Vranes, Jason Park, Jay Mahadeokar, Jeet Shah, Jelmer van der Linde, Jennifer Billock, Jenny Hong, Jenya Lee, Jeremy Fu, Jianfeng Chi, Jianyu Huang, Jiawen Liu, Jie Wang, Jiecao Yu, Joanna Bitton, Joe Spisak, Jongsoo Park, Joseph Rocca, Joshua Johnston, Joshua Saxe, Junteng Jia, Kalyan Vasuden Alwala, Kartikeya Upasani, Kate Plawiak, Ke Li, Kenneth Heafield, Kevin Stone, and et al. The llama 3 herd of models. *CoRR*, abs/2407.21783, 2024. 2
- [11] Yuval Eldar, Michael Lindenbaum, Moshe Porat, and Yehoshua Y. Zeevi. The farthest point strategy for progressive image sampling. *IEEE Trans. Image Process.*, 6(9): 1305–1315, 1997. 3
- [12] Patrick Esser, Robin Rombach, and Björn Ommer. Taming transformers for high-resolution image synthesis. In *IEEE Conference on Computer Vision and Pattern Recognition, CVPR 2021, virtual, June 19-25, 2021*, pages 12873–12883. Computer Vision Foundation / IEEE, 2021. 2
- [13] Wanquan Feng, Jin Li, Hongrui Cai, Xiaonan Luo, and Juyong Zhang. Neural points: Point cloud representation with neural fields for arbitrary upsampling. In *IEEE/CVF Conference on Computer Vision and Pattern Recognition, CVPR 2022, New Orleans, LA, USA, June 18-24, 2022*, pages 18612–18621. IEEE, 2022. 3
- [14] Will Grathwohl, Ricky T. Q. Chen, Jesse Bettencourt, Ilya Sutskever, and David Duvenaud. FFJORD: free-form continuous dynamics for scalable reversible generative models. In *7th International Conference on Learning Representations, ICLR 2019, New Orleans, LA, USA, May 6-9, 2019*. OpenReview.net, 2019. 3
- [15] Yun He, Danhang Tang, Yinda Zhang, Xiangyang Xue, and Yanwei Fu. Grad-pu: Arbitrary-scale point cloud upsampling via gradient descent with learned distance functions. In *IEEE/CVF Conference on Computer Vision and Pattern Recognition, CVPR 2023, Vancouver, BC, Canada, June 17-24, 2023*, pages 5354–5363. IEEE, 2023. 3

- [16] Jonathan Ho, Ajay Jain, and Pieter Abbeel. Denoising diffusion probabilistic models. In *Advances in Neural Information Processing Systems 33: Annual Conference on Neural Information Processing Systems 2020, NeurIPS 2020, December 6-12, 2020, virtual*, 2020. 3
- [17] Le Hui, Rui Xu, Jin Xie, Jianjun Qian, and Jian Yang. Progressive point cloud deconvolution generation network. In *Computer Vision - ECCV 2020 - 16th European Conference, Glasgow, UK, August 23-28, 2020, Proceedings, Part XV*, pages 397–413. Springer, 2020. 3
- [18] Hyeongju Kim, Hyeonseung Lee, Woo Hyun Kang, Joun Yeop Lee, and Nam Soo Kim. Softflow: Probabilistic framework for normalizing flow on manifolds. In *Advances in Neural Information Processing Systems 33: Annual Conference on Neural Information Processing Systems 2020, NeurIPS 2020, December 6-12, 2020, virtual*, 2020. 3, 4
- [19] Jinwoo Kim, Jaehoon Yoo, Juho Lee, and Seunghoon Hong. Setvae: Learning hierarchical composition for generative modeling of set-structured data. In *IEEE Conference on Computer Vision and Pattern Recognition, CVPR 2021, virtual, June 19-25, 2021*, pages 15059–15068. Computer Vision Foundation / IEEE, 2021. 3, 4
- [20] Roman Klokov, Edmond Boyer, and Jakob Verbeek. Discrete point flow networks for efficient point cloud generation. In *Computer Vision - ECCV 2020 - 16th European Conference, Glasgow, UK, August 23-28, 2020, Proceedings, Part XXIII*, pages 694–710. Springer, 2020. 3, 4
- [21] Doyup Lee, Chiheon Kim, Saehoon Kim, Minsu Cho, and Wook-Shin Han. Autoregressive image generation using residual quantization. In *IEEE/CVF Conference on Computer Vision and Pattern Recognition, CVPR 2022, New Orleans, LA, USA, June 18-24, 2022*, pages 11513–11522. IEEE, 2022. 2, 3
- [22] Jiabao Lei, Kewei Shi, Zhihao Liang, and Kui Jia. Armesh: Autoregressive mesh generation via next-level-of-detail prediction, 2025. 3
- [23] Ruihui Li, Xianzhi Li, Chi-Wing Fu, Daniel Cohen-Or, and Pheng-Ann Heng. PU-GAN: A point cloud upsampling adversarial network. In *2019 IEEE/CVF International Conference on Computer Vision, ICCV 2019, Seoul, Korea (South), October 27 - November 2, 2019*, pages 7202–7211. IEEE, 2019. 3
- [24] Ruihui Li, Xianzhi Li, Pheng-Ann Heng, and Chi-Wing Fu. Point cloud upsampling via disentangled refinement. In *IEEE Conference on Computer Vision and Pattern Recognition, CVPR 2021, virtual, June 19-25, 2021*, pages 344–353. Computer Vision Foundation / IEEE, 2021. 3
- [25] Yaron Lipman, Ricky T. Q. Chen, Heli Ben-Hamu, Maximilian Nickel, and Matthew Le. Flow matching for generative modeling. In *The Eleventh International Conference on Learning Representations, ICLR 2023, Kigali, Rwanda, May 1-5, 2023*. OpenReview.net, 2023. 3
- [26] Hao Liu, Hui Yuan, Junhui Hou, Raouf Hamzaoui, and Wei Gao. PUFA-GAN: A frequency-aware generative adversarial network for 3d point cloud upsampling. *IEEE Trans. Image Process.*, 31:7389–7402, 2022. 3
- [27] Xingchao Liu, Chengyue Gong, and Qiang Liu. Flow straight and fast: Learning to generate and transfer data with rectified flow. In *The Eleventh International Conference on Learning Representations, ICLR 2023, Kigali, Rwanda, May 1-5, 2023*. OpenReview.net, 2023. 3
- [28] Zhijian Liu, Haotian Tang, Yujun Lin, and Song Han. Point-voxel CNN for efficient 3d deep learning. In *Advances in Neural Information Processing Systems 32: Annual Conference on Neural Information Processing Systems 2019, NeurIPS 2019, December 8-14, 2019, Vancouver, BC, Canada*, pages 963–973, 2019. 4
- [29] David Lopez-Paz and Maxime Oquab. Revisiting classifier two-sample tests. In *5th International Conference on Learning Representations, ICLR 2017, Toulon, France, April 24-26, 2017, Conference Track Proceedings*. OpenReview.net, 2017. 6
- [30] Cheng Lu, Yuhao Zhou, Fan Bao, Jianfei Chen, Chongxuan Li, and Jun Zhu. Dpm-solver: A fast ODE solver for diffusion probabilistic model sampling in around 10 steps. In *Advances in Neural Information Processing Systems 35: Annual Conference on Neural Information Processing Systems 2022, NeurIPS 2022, New Orleans, LA, USA, November 28 - December 9, 2022*, 2022. 1
- [31] David Luebke, Martin Reddy, Jonathan D. Cohen, Amitabh Varshney, Benjamin Watson, and Robert Huebner. Level of detail for 3d graphics. In *level of detail for 3d graphics*. Morgan Kaufmann, San Francisco, 2003. 2
- [32] Luqing Luo, Lulu Tang, Wanyi Zhou, Shizheng Wang, and Zhi-Xin Yang. PU-EVA: an edge-vector based approximation solution for flexible-scale point cloud upsampling. In *2021 IEEE/CVF International Conference on Computer Vision, ICCV 2021, Montreal, QC, Canada, October 10-17, 2021*, pages 16188–16197. IEEE, 2021. 3
- [33] Shitong Luo and Wei Hu. Diffusion probabilistic models for 3d point cloud generation. In *IEEE Conference on Computer Vision and Pattern Recognition, CVPR 2021, virtual, June 19-25, 2021*, pages 2837–2845. Computer Vision Foundation / IEEE, 2021. 2, 3, 6, 4
- [34] Paritosh Mittal, Yen-Chi Cheng, Maneesh Singh, and Shubham Tulsiani. Autosdf: Shape priors for 3d completion, reconstruction and generation. In *IEEE/CVF Conference on Computer Vision and Pattern Recognition, CVPR 2022, New Orleans, LA, USA, June 18-24, 2022*, pages 306–315. IEEE, 2022. 2
- [35] Shentong Mo, Enze Xie, Ruihang Chu, Lanqing Hong, Matthias Nießner, and Zhenguo Li. Dit-3d: Exploring plain diffusion transformers for 3d shape generation. In *Advances in Neural Information Processing Systems 36: Annual Conference on Neural Information Processing Systems 2023, NeurIPS 2023, New Orleans, LA, USA, December 10 - 16, 2023*, 2023. 3, 4
- [36] OpenAI. GPT-4 technical report. *CoRR*, abs/2303.08774, 2023. 2
- [37] Ajay Patel, Bryan Li, Mohammad Sadegh Rasooli, Noah Constant, Colin Raffel, and Chris Callison-Burch. Bidirectional language models are also few-shot learners. In *The Eleventh International Conference on Learning Representa-*

- tions, *ICLR 2023, Kigali, Rwanda, May 1-5, 2023*. OpenReview.net, 2023. 2
- [38] Charles Ruizhongtai Qi, Hao Su, Kaichun Mo, and Leonidas J. Guibas. Pointnet: Deep learning on point sets for 3d classification and segmentation. In *2017 IEEE Conference on Computer Vision and Pattern Recognition, CVPR 2017, Honolulu, HI, USA, July 21-26, 2017*, pages 77–85. IEEE Computer Society, 2017. 1, 4
- [39] Charles Ruizhongtai Qi, Li Yi, Hao Su, and Leonidas J. Guibas. Pointnet++: Deep hierarchical feature learning on point sets in a metric space. In *Advances in Neural Information Processing Systems 30: Annual Conference on Neural Information Processing Systems 2017, December 4-9, 2017, Long Beach, CA, USA*, pages 5099–5108, 2017. 1, 4
- [40] Guocheng Qian, Abdullellah Abualshour, Guohao Li, Ali K. Thabet, and Bernard Ghanem. PU-GCN: point cloud upsampling using graph convolutional networks. In *IEEE Conference on Computer Vision and Pattern Recognition, CVPR 2021, virtual, June 19-25, 2021*, pages 11683–11692. Computer Vision Foundation / IEEE, 2021. 3
- [41] Guocheng Qian, Yuchen Li, Houwen Peng, Jinjie Mai, Hasan Hammoud, Mohamed Elhoseiny, and Bernard Ghanem. Pointnext: Revisiting pointnet++ with improved training and scaling strategies. In *Advances in Neural Information Processing Systems 35: Annual Conference on Neural Information Processing Systems 2022, NeurIPS 2022, New Orleans, LA, USA, November 28 - December 9, 2022*. 4
- [42] Yue Qian, Junhui Hou, Sam Kwong, and Ying He. Pugeonet: A geometry-centric network for 3d point cloud upsampling. In *Computer Vision - ECCV 2020 - 16th European Conference, Glasgow, UK, August 23-28, 2020, Proceedings, Part XIX*, pages 752–769. Springer, 2020. 3
- [43] Yue Qian, Junhui Hou, Sam Kwong, and Ying He. Deep magnification-flexible upsampling over 3d point clouds. *IEEE Trans. Image Process.*, 30:8354–8367, 2021. 3
- [44] Shi Qiu, Saeed Anwar, and Nick Barnes. Pu-transformer: Point cloud upsampling transformer. In *Computer Vision - ACCV 2022 - 16th Asian Conference on Computer Vision, Macao, China, December 4-8, 2022, Proceedings, Part I*, pages 326–343. Springer, 2022. 3
- [45] Wentao Qu, Yuantian Shao, Lingwu Meng, Xiaoshui Huang, and Liang Xiao. A conditional denoising diffusion probabilistic model for point cloud upsampling. In *IEEE/CVF Conference on Computer Vision and Pattern Recognition, CVPR 2024, Seattle, WA, USA, June 16-22, 2024*, pages 20786–20795. IEEE, 2024. 3, 4
- [46] Zhiyuan Ren, Minchul Kim, Feng Liu, and Xiaoming Liu. TIGER: time-varying denoising model for 3d point cloud generation with diffusion process. In *IEEE/CVF Conference on Computer Vision and Pattern Recognition, CVPR 2024, Seattle, WA, USA, June 16-22, 2024*, pages 9462–9471. IEEE, 2024. 1, 2, 3, 6, 4
- [47] Danilo Jimenez Rezende and Shakir Mohamed. Variational inference with normalizing flows. In *Proceedings of the 32nd International Conference on Machine Learning, ICML 2015, Lille, France, 6-11 July 2015*, pages 1530–1538. JMLR.org, 2015. 3
- [48] Dong Wook Shu, Sung Woo Park, and Junseok Kwon. 3d point cloud generative adversarial network based on tree structured graph convolutions. In *2019 IEEE/CVF International Conference on Computer Vision, ICCV 2019, Seoul, Korea (South), October 27 - November 2, 2019*, pages 3858–3867. IEEE, 2019. 3
- [49] Jiaming Song, Chenlin Meng, and Stefano Ermon. Denoising diffusion implicit models. In *9th International Conference on Learning Representations, ICLR 2021, Virtual Event, Austria, May 3-7, 2021*. OpenReview.net, 2021. 1, 3, 4
- [50] Yang Song, Jascha Sohl-Dickstein, Diederik P. Kingma, Abhishek Kumar, Stefano Ermon, and Ben Poole. Score-based generative modeling through stochastic differential equations. In *9th International Conference on Learning Representations, ICLR 2021, Virtual Event, Austria, May 3-7, 2021*. OpenReview.net, 2021. 3
- [51] Yongbin Sun, Yue Wang, Ziwei Liu, Joshua E. Siegel, and Sanjay E. Sarma. Pointgrow: Autoregressively learned point cloud generation with self-attention. In *IEEE Winter Conference on Applications of Computer Vision, WACV 2020, Snowmass Village, CO, USA, March 1-5, 2020*, pages 61–70. IEEE, 2020. 2, 3, 6, 7, 4
- [52] Chameleon Team. Chameleon: Mixed-modal early-fusion foundation models. *CoRR*, abs/2405.09818, 2024. 2
- [53] Keyu Tian, Yi Jiang, Zehuan Yuan, Bingyue Peng, and Liwei Wang. Visual autoregressive modeling: Scalable image generation via next-scale prediction. *CoRR*, abs/2404.02905, 2024. 3, 1
- [54] Aaron van den Oord, Oriol Vinyals, and koray kavukcuoglu. Neural discrete representation learning. In *Advances in Neural Information Processing Systems*. Curran Associates, Inc., 2017. 3
- [55] Jionghao Wang, Cheng Lin, Yuan Liu, Rui Xu, Zhiyang Dou, Xiaoxiao Long, Haoxiang Guo, Taku Komura, Wenping Wang, and Xin Li. Pdt: Point distribution transformation with diffusion models. In *Proceedings of the Special Interest Group on Computer Graphics and Interactive Techniques Conference Conference Papers*, pages 1–11, 2025. 3
- [56] Haibin Wu, Kai-Wei Chang, Yuan-Kuei Wu, and Hung-yi Lee. Speechgen: Unlocking the generative power of speech language models with prompts. *CoRR*, abs/2306.02207, 2023. 2
- [57] Lemeng Wu, Dilin Wang, Chengyue Gong, Xingchao Liu, Yunyang Xiong, Rakesh Ranjan, Raghuraman Krishnamoorthi, Vikas Chandra, and Qiang Liu. Fast point cloud generation with straight flows. In *IEEE/CVF Conference on Computer Vision and Pattern Recognition, CVPR 2023, Vancouver, BC, Canada, June 17-24, 2023*, pages 9445–9454. IEEE, 2023. 3, 4
- [58] Xiaoyang Wu, Yixing Lao, Li Jiang, Xihui Liu, and Hengshuang Zhao. Point transformer V2: grouped vector attention and partition-based pooling. In *Advances in Neural Information Processing Systems 35: Annual Conference on Neural Information Processing Systems 2022, NeurIPS 2022, New Orleans, LA, USA, November 28 - December 9, 2022*, 2022. 2

- [59] Xiaoyang Wu, Li Jiang, Peng-Shuai Wang, Zhijian Liu, Xihui Liu, Yu Qiao, Wanli Ouyang, Tong He, and Hengshuang Zhao. Point transformer V3: simpler, faster, stronger. In *IEEE/CVF Conference on Computer Vision and Pattern Recognition, CVPR 2024, Seattle, WA, USA, June 16-22, 2024*, pages 4840–4851. IEEE, 2024. [2](#)
- [60] Xingguang Yan, Liqiang Lin, Niloy J. Mitra, Dani Lischinski, Daniel Cohen-Or, and Hui Huang. Shapeformer: Transformer-based shape completion via sparse representation. In *IEEE/CVF Conference on Computer Vision and Pattern Recognition, CVPR 2022, New Orleans, LA, USA, June 18-24, 2022*, pages 6229–6239. IEEE, 2022. [2](#)
- [61] Guandao Yang, Xun Huang, Zekun Hao, Ming-Yu Liu, Serge J. Belongie, and Bharath Hariharan. Pointflow: 3d point cloud generation with continuous normalizing flows. In *2019 IEEE/CVF International Conference on Computer Vision, ICCV 2019, Seoul, Korea (South), October 27 - November 2, 2019*, pages 4540–4549. IEEE, 2019. [3](#), [6](#), [4](#)
- [62] Lequan Yu, Xianzhi Li, Chi-Wing Fu, Daniel Cohen-Or, and Pheng-Ann Heng. Pu-net: Point cloud upsampling network. In *2018 IEEE Conference on Computer Vision and Pattern Recognition, CVPR 2018, Salt Lake City, UT, USA, June 18-22, 2018*, pages 2790–2799. Computer Vision Foundation / IEEE Computer Society, 2018. [3](#), [4](#)
- [63] Manzil Zaheer, Satwik Kottur, Siamak Ravanbakhsh, Barnabás Póczos, Ruslan Salakhutdinov, and Alexander J. Smola. Deep sets. In *Advances in Neural Information Processing Systems 30: Annual Conference on Neural Information Processing Systems 2017, December 4-9, 2017, Long Beach, CA, USA*, pages 3391–3401, 2017. [1](#)
- [64] Xiaohui Zeng, Arash Vahdat, Francis Williams, Zan Gojic, Or Litany, Sanja Fidler, and Karsten Kreis. LION: latent point diffusion models for 3d shape generation. In *Advances in Neural Information Processing Systems 35: Annual Conference on Neural Information Processing Systems 2022, NeurIPS 2022, New Orleans, LA, USA, November 28 - December 9, 2022*, 2022. [1](#), [2](#), [3](#), [6](#), [7](#), [4](#)
- [65] Dong Zhang, Shimin Li, Xin Zhang, Jun Zhan, Pengyu Wang, Yaqian Zhou, and Xipeng Qiu. Speechgpt: Empowering large language models with intrinsic cross-modal conversational abilities. In *Findings of the Association for Computational Linguistics: EMNLP 2023, Singapore, December 6-10, 2023*, pages 15757–15773. Association for Computational Linguistics, 2023. [2](#)
- [66] Hengshuang Zhao, Li Jiang, Jiaya Jia, Philip H. S. Torr, and Vladlen Koltun. Point transformer. In *2021 IEEE/CVF International Conference on Computer Vision, ICCV 2021, Montreal, QC, Canada, October 10-17, 2021*, pages 16239–16248. IEEE, 2021. [2](#)
- [67] Chunting Zhou, Lili Yu, Arun Babu, Kushal Tirumala, Michihiro Yasunaga, Leonid Shamis, Jacob Kahn, Xuezhe Ma, Luke Zettlemoyer, and Omer Levy. Transfusion: Predict the next token and diffuse images with one multi-modal model, 2024. [2](#)
- [68] Linqi Zhou, Yilun Du, and Jiajun Wu. 3d shape generation and completion through point-voxel diffusion. In *2021 IEEE/CVF International Conference on Computer Vision,*
- ICCV 2021, Montreal, QC, Canada, October 10-17, 2021*, pages 5806–5815. IEEE, 2021. [1](#), [2](#), [3](#), [6](#), [8](#), [4](#)

PointNSP: Autoregressive 3D Point Cloud Generation with Next-Scale Level-of-Detail Prediction

Supplementary Material

6. Permutation Invariance of Probability Distribution

Here we show why the distribution $p(\mathbf{X}_1, \mathbf{X}_2, \dots, \mathbf{X}_K) = \prod_{k=1}^K p(\mathbf{X}_k | \mathbf{X}_{k-1}, \dots, \mathbf{X}_2, \mathbf{X}_1)$ in Eq. 3 preserves the permutation invariance property $p(\pi(\mathbf{x}_1, \dots, \mathbf{x}_N)) = p(\mathbf{x}_1, \dots, \mathbf{x}_N), \forall \pi \in S_N$ in Eq. 2.

By definition, the joint distribution factorizes as:

$$p(\mathbf{X}_1, \mathbf{X}_2, \dots, \mathbf{X}_K) = p(\mathbf{X}_1)p(\mathbf{X}_2|\mathbf{X}_1) \dots p(\mathbf{X}_K|\mathbf{X}_1, \dots, \mathbf{X}_{K-1}). \quad (10)$$

Consider an arbitrary permutation π acting on the full set of points $\mathbf{X} = \bigcup_{k=1}^K \mathbf{X}_k$. This permutation can be decomposed into independent permutations within each scale:

$$\pi = (\pi_1, \pi_2, \dots, \pi_K), \quad \pi_k \in S_{s_k}. \quad (11)$$

Then we aim to prove that:

$$p(\pi_1(\mathbf{X}_1), \dots, \pi_K(\mathbf{X}_K)) = p(\mathbf{X}_1, \dots, \mathbf{X}_K). \quad (12)$$

Recall that FPS is permutation-invariant, the resulting LoD sampling sequence $(\mathbf{X}_1, \dots, \mathbf{X}_K)$ is *permutation-invariant* (its inherent stochasticity operates at the set level and is independent of point ordering). The core components of *PointNSP* —namely the feature encoder $\mathcal{E}(\cdot)$, upsampling, query, and the decoder $D(\cdot)$ —are all *permutation-equivariant*, ensuring that each output feature remains aligned with its corresponding input point. Therefore, the mapping between \mathbf{X}_k and conditioning context shapes $(\mathbf{X}_1, \dots, \mathbf{X}_{k-1})$ remains unchanged with respect to any global permutation π . Then, for any permutation π_k of points within \mathbf{X}_k :

$$p(\pi_k(\mathbf{X}_k) | \pi_1(\mathbf{X}_1), \dots, \pi_{k-1}(\mathbf{X}_{k-1})) = p(\mathbf{X}_k | \mathbf{X}_1, \dots, \mathbf{X}_{k-1}). \quad (13)$$

This holds for each $k = 1, \dots, K$. Then the joint distribution under these permutations is

$$\begin{aligned} & p(\pi_1(\mathbf{X}_1), \dots, \pi_K(\mathbf{X}_K)) \\ &= \prod_{k=1}^K p(\pi_k(\mathbf{X}_k) | \pi_1(\mathbf{X}_1), \dots, \pi_{k-1}(\mathbf{X}_{k-1})) \\ &= \prod_{k=1}^K p(\mathbf{X}_k | \mathbf{X}_{k-1}, \dots, \mathbf{X}_2, \mathbf{X}_1) \\ &= p(\mathbf{X}_1, \dots, \mathbf{X}_K) \end{aligned} \quad (14)$$

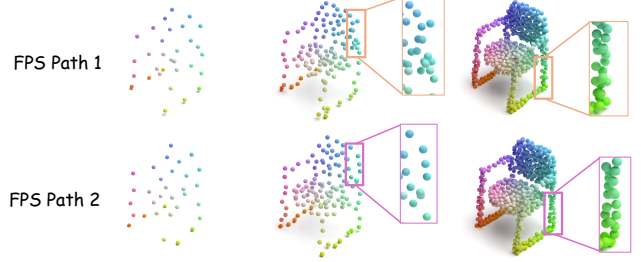


Figure S1. Illustration of different LoD sequences for a single shape. Owing to the inherent stochasticity of the sampling strategy in Eq. 17, our method naturally produces *diverse causal LoD sequences* for the same 3D shape across training epochs. At each scale, these variations encourage *broader spatial coverage* of the underlying geometry, thereby enhancing learning robustness.

Consequently, the autoregressive factorization preserves permutation invariance: permuting the points within any scale does not change the resulting joint probability:

$$p(\pi(\mathbf{x}_1, \dots, \mathbf{x}_N)) = p(\mathbf{x}_1, \dots, \mathbf{x}_N), \forall \pi \in S_N. \quad (15)$$

7. Algorithm Details

LoD Sequence Sampling. This step is a core component of *PointNSP* training, and we provide additional details here to eliminate any potential ambiguity. If one were to directly apply the original image-based VAR framework [53] to 3D point clouds, latent features for sampled LoD sequences would be obtained via

$$\mathbf{f}_k = \text{FPS}(\mathbf{f}^{k-2} - \tilde{\mathbf{f}}_{k-1}), \mathbf{f}_1 = \text{FPS}(\mathbf{f}^0). \quad (16)$$

However, this strategy is unsuitable for 3D point clouds. Applying FPS directly in latent space implicitly assumes that latent distances form a meaningful metric, yet these distances need not correlate with underlying geometric structure. As a result, sampling in latent space cannot reliably preserve geometric uniformity or spatial coverage. To address this, rather than iteratively applying FPS in latent space, we apply FPS in Euclidean 3D space in a *fine-to-coarse* manner:

$$\mathbf{X}_{k-1} = \text{FPS}(\mathbf{X}_k), \mathbf{X}_K = \mathbf{X}. \quad (17)$$

This produces a geometrically consistent LoD sequence $(\mathbf{X}_1, \dots, \mathbf{X}_K)$ from coarse to fine, with guaranteed point correspondences $\mathbf{X}_1 \subsetneq \dots \subsetneq \mathbf{X}_{K-1} \subsetneq \mathbf{X}_K$. We then obtain latent features by querying the indices mapping each

\mathbf{X}_k back to the original point set:

$$\mathbf{f}_k = \text{query}(\mathbf{f}^{k-2} - \tilde{\mathbf{f}}_{k-1}, \mathbf{X}_k), \mathbf{f}_1 = \text{query}(\mathbf{f}^0, \mathbf{X}_1), \quad (18)$$

where $\mathbf{f}^0 = \mathcal{E}(\mathbf{X})$. This is Eq. 4. Here we need to emphasize that the LoD sequence $(\mathbf{X}_1, \dots, \mathbf{X}_K)$ is constructed in advance following Eq. 17 and the Line 5 ($\mathbf{X}_k = \text{FPS}(\mathbf{X}, s_k)$) in Algorithm 1 denotes that \mathbf{X}_k with scale s_k is obtained starting from \mathbf{X} . Note that it does not mean the \mathbf{X}_k is obtained by directly applying FPS on the original \mathbf{X} as this would break the point correspondence across scales (i.e. $\mathbf{X}_i \cap \mathbf{X}_j \neq \mathbf{X}_i, i < j$). Since FPS is inherently stochastic due to its random initialization, we can naturally obtain diverse LoD sequences for each shape \mathbf{X} across training epochs. This variability is desirable, as the refinement path need not be unique; sampling multiple paths improves spatial coverage, as discussed in Section 3.2. For example, for epoch 0 and epoch 1, we may obtain two LoD sequences for shape \mathbf{X} :

$$(\mathbf{X}_1^0, \dots, \mathbf{X}_K^0), (\mathbf{X}_1^1, \dots, \mathbf{X}_K^1). \quad (19)$$

At each scale, \mathbf{X}_k^0 and \mathbf{X}_k^1 represent the same underlying surface but with different point coverages, which helps improve learning robustness and generalization. We illustrate this LoD sequence sampling issue in Figure S1.

Coordinate-based Positional Encoding. We adopt the absolute positional encoding strategy purely based on 3D coordinates used in TIGER [46]. Based on our experiments, we find the Base λ Position Encoding (B λ PE) performs better and here we present its formula:

$$p = \lambda^2 * z_i + \lambda * y_i + x_i \quad (20)$$

$$\mathbf{P}_k(p, 2i) = \sin\left(\frac{p}{10000^{\frac{2i}{D}}}\right) \quad (21)$$

$$\mathbf{P}_k(p, 2i + 1) = \cos\left(\frac{p}{10000^{\frac{2i}{D}}}\right), \quad (22)$$

where $\mathbf{x}_i = \mathbf{X}_k[i] = (x_i, y_i, z_i) \in \mathbb{R}^3$, p is a polynomial expression with hyperparameter coefficient λ . We set $\lambda = 1000$ following the setting in TIGER [46], which means this preserves three decimal places of precision. Here $\mathbf{P}_k \in \mathbb{R}^{s_k \times d}$ denotes the positional embedding of all tokens within the scale k . In short, we apply the B λ PE embedding strategy scale-by-scale.

Intra-Scale Token Embedding. Instead of simply adding all token embeddings together, the real implementation is analogous to Llama [10] by adding positional embedding and scale embedding to query and key vectors. Specifically, we retrieve the codebook embedding \mathbf{z}_k for each scale token q_k and then upsampled from input scale to output scale

($s_k \rightarrow s_{k+1}$): $\mathbf{z}_k = \text{upsampling}(\mathbf{z}_k) \in \mathbb{R}^{s_{k+1} \times d}$ following the Eq. 6. Positional embedding $\mathbf{p}_k^i = \mathbf{P}_k[i]$ for each token q_k^i is derived with from the decoded intermediate structure \mathbf{X}_k as described in Eq. 9. During inference stage, the intermediate structure $\tilde{\mathbf{X}}_k$ is decoded using the predicted token \hat{q}_k instead. Additionally, the model needs to know which scale that each token belongs to. Therefore, s_k is a simple one-hot embedding $\mathbf{s}_k = \text{one-hot-embedding}(k)$ out of total K scales. Tokens from the same scale k share the same scale embedding \mathbf{s}_k ($\mathbf{s}_k^i = \mathbf{s}_k^j$ for q_k^i, q_k^j). For all input scale tokens, we add both the positional embedding \mathbf{p}_k^i and the scale embedding \mathbf{s}_k^i to the query \mathbf{u}_k^i and key vectors \mathbf{v}_k^i derived in the attention mechanism:

$$\mathbf{u}_k^i = \mathbf{W}_U \mathbf{z}_k^i + \mathbf{p}_k^i + \mathbf{s}_k^i, \mathbf{v}_k^i = \mathbf{W}_V \mathbf{z}_k^i + \mathbf{p}_k^i + \mathbf{s}_k^i, \quad (23)$$

where \mathbf{W}_U and \mathbf{W}_V are projection matrices for queries and keys respectively. Together with value vectors, these vectors will be fed to the block-wise causal transformer for next-scale token prediction.

8. Hyperparameters & Reproducibility Settings

Hyperparameters & Reproducibility Settings. Specifically, we set the learning rate $3e^{-4}$ and the batch-size 32. We perform all the experiments on a workstation with Intel Xeon Gold 6154 CPU (3.00GHz) and 8 NVIDIA Tesla V100 (32GB) GPUs. We use an AdamW optimizer with an initial learning rate of 10^{-4} for VQVAE training and 10^{-3} for autoregressive transformer training respectively. For up-sampling and completion experiments, we follow the experimental settings of PVD [68]. For many-class generation, we mainly inherit the experimental setting from LION [64].

Hyperparameter	Value
# PVCNN layers	4
# PVCNN hidden dimension	1024
# PVCNN voxel grid size	32
# MLP layers	6
# Attention dimension	1024
# Attention head	32
Optimizer	AdamW
Weight Decay	0.01
LR Schedule	Cosine

The effect of # scales K . Figure S2 illustrates the impact of the total number of scales on the overall performance of *PointNSP*. As the number of scales increases, *PointNSP*'s performance improves accordingly. However, beyond $K = 11$ scales, no further performance gains are observed. We hypothesize that additional scales may require higher point cloud densities to be effective. Moreover, increasing the number of scales naturally leads to longer sampling times.

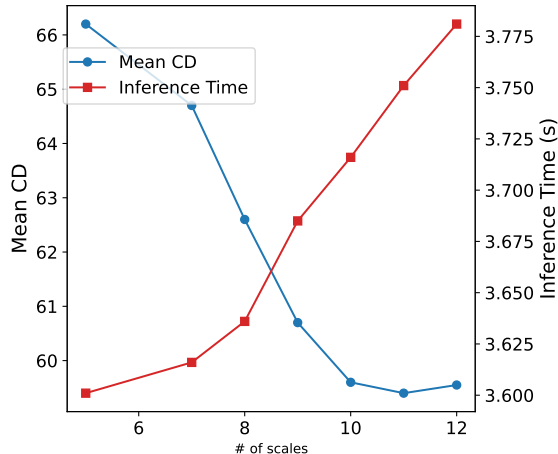


Figure S2. The effect of number of scales on the overall performance of *PointNSP*.

9. More Experimental Results

Due to page limitations, the main paper reports only the strongest baseline methods in the primary comparison table. Here, we provide a more comprehensive evaluation that additionally includes 1-GAN [1] (GAN-based), PointFlow [61], DPF-Net [20], SoftFlow [18] (normalizing flow-based), SetVAE [19] (VAE-based), PVD-DDIM [49] (diffusion models with advanced samplers), PSF [57] (flow-matching-based), and DIT-3D [35]. We include only methods with publicly available implementations or those reporting explicit quantitative results in their original papers. Please see Table S3 for comprehensive comparisons.

Since ShapeNet categories are highly imbalanced, prior works typically report results only on the three largest categories—airplane, chair, and car—while the remaining categories contain significantly fewer samples. To provide a more comprehensive evaluation, we additionally report performance on three smaller categories: table, sofa, and lamp. As shown in Table S1, *PointNSP* consistently and substantially outperforms all baseline methods, demonstrating its strong learning efficiency *under limited data conditions*.

Model	Table	Sofa	Lamp
	CD / EMD	CD / EMD	CD / EMD
PointFlow [61]	92.3 / 92.8	85.6 / 88.4	88.7 / 98.5
PointGPT [4]	91.5 / 90.9	83.8 / 88.4	88.7 / 98.5
ShapeGF [2]	83.7 / 81.5	79.2 / 81.3	86.4 / 86.8
PVD [68]	76.8 / 80.2	73.5 / 96.7	89.1 / 89.4
LION [64]	68.4 / 78.7	67.9 / 90.2	81.3 / 82.6
<i>PointNSP-m</i>	61.2 / 76.5	60.8 / 83.7	73.9 / 74.8

Table S1. Per-category generation quality on ShapeNet. We report 1-NNA CD/EMD (\downarrow) on **Table**, **Sofa**, and **Lamp**. Best in **bold**, second best underlined.

In addition to the 55-class generation setting, we also evaluate the 13-class setting used in LION [64]. The results, presented in Table S2, show that *PointNSP* achieves state-of-the-art generation quality.

Model	CD \downarrow	EMD \downarrow
TreeGAN [48]	96.80	96.60
PointFlow [61]	63.25	66.05
ShapeGF [2]	55.65	59.00
SetVAE [19]	79.25	95.25
PDGN [17]	71.05	86.00
DPF-Net [20]	67.10	64.75
DPM [33]	62.30	86.50
PVD [68]	58.65	57.85
LION [64]	<u>55.52</u>	<u>53.89</u>
<i>PointNSP-m</i>	54.70	52.82

Table S2. Generation results (1-NNA \downarrow) trained jointly on 13 classes of ShapeNet-vol.

10. More Visualization Results

We showcase diverse 3D point clouds generated by *PointNSP* across a wide variety of shapes (Figures S3 and S4). Additional single-class generation results for five categories are provided in Figures S5–S9. We further illustrate the multi-scale sequential generation process in Figures S10–S11, and present more examples of point cloud completion and upsampling in Figures S13 and S12.

11. Other Related Works

Point Cloud Upsampling. Point cloud upsampling is a crucial process in 3D modeling, aimed at increasing the resolution of low-resolution 3D point clouds. PU-Net [62] pioneered the use of deep neural networks for this task, laying the foundation for subsequent advancements. Models such as PU-GCN [40] and PU-Transformer [44] have further refined point cloud feature extraction by leveraging graph convolutional networks and transformer networks, respectively. Additionally, approaches like Dis-PU [24], PU-EVA [32], and MPU [9] have enhanced the PU-Net pipeline by incorporating cascading refinement architectures. Other methods, such as PUGeo-Net [42], NePs [13], and MAFU [43], employ local geometry projections into 2D space to model the underlying 3D surface. More recent approaches have reframed upsampling as a generation task. For instance, PU-GAN [23] and PUFA-GAN [26] leverage generative adversarial networks (GANs) to produce high-resolution point clouds. Grad-PU [15] first generates coarse dense point clouds through nearest-point interpolation and then refines them iteratively using diffusion

Table S3. The *Performance* (1-NNA) is evaluated based on single-class generation. The second block specifies the types of generative models used in each study. The best performance is highlighted in **bold**, while the second-best performance is underlined. Performance is reported on two dataset splits: the top corresponds to the random split, and the bottom corresponds to the LION split.

Model	Generative Model	Airplane		Chair		Car		Mean CD ↓	Mean EMD ↓
		CD ↓	EMD ↓	CD ↓	EMD ↓	CD ↓	EMD ↓		
1-GAN [1]	GAN	87.30	93.95	68.58	83.84	66.49	88.78	74.12	88.86
PointFlow [61]	Normalizing Flow	75.68	70.74	62.84	60.57	58.10	56.25	65.54	62.52
DPF-Net [20]	Normalizing Flow	75.18	65.55	62.00	58.53	62.35	54.48	66.51	59.52
SoftFlow [18]	Normalizing Flow	76.05	65.80	59.21	60.05	64.77	60.09	66.67	61.98
SetVAE [19]	VAE	75.31	77.65	58.76	61.48	59.66	61.48	64.58	66.87
ShapeGF [2]	Diffusion	80.00	76.17	68.96	65.48	63.20	56.53	70.72	66.06
DPM [33]	Diffusion	76.42	86.91	60.05	74.77	68.89	79.97	68.45	80.55
PVD-DDIM [49]	Diffusion	76.21	69.84	61.54	57.73	60.95	59.35	66.23	62.31
PSF [57]	Diffusion	74.45	67.54	58.92	54.45	57.19	56.07	62.41	57.20
PVD [68]	Diffusion	73.82	64.81	56.26	53.32	54.55	53.83	61.54	57.32
LION [64]	Diffusion	72.99	64.21	55.67	53.82	53.47	53.21	61.75	57.59
DIT-3D [35]	Diffusion	-	-	54.58	53.21	-	-	-	-
TIGER [46]	Diffusion	73.02	64.10	55.15	53.18	53.21	53.95	60.46	57.08
PointGrow [51]	Autoregressive	82.20	78.54	63.14	61.87	67.56	65.89	70.96	68.77
CanonicalVAE [7]	Autoregressive	80.15	76.27	62.78	61.05	63.23	61.56	68.72	66.29
PointGPT [4]	Autoregressive	74.85	65.61	57.24	55.01	55.91	54.24	63.44	62.24
<i>PointNSP-s (ours)</i>	Autoregressive	<u>72.92</u>	<u>63.98</u>	54.89	<u>53.02</u>	<u>52.86</u>	<u>52.07</u>	60.22	56.36
<i>PointNSP-m (ours)</i>	Autoregressive	72.24	63.69	54.54	52.85	52.17	51.85	59.65	56.13
LION	Diffusion	67.41	61.23	<u>53.70</u>	52.34	<u>53.41</u>	51.14	<u>58.17</u>	54.90
TIGER	Diffusion	67.21	56.26	54.32	51.71	54.12	50.24	58.55	52.74
<i>PointNSP-s (ours)</i>	Autoregressive	<u>67.15</u>	<u>56.12</u>	54.22	<u>51.19</u>	53.98	<u>50.15</u>	58.45	<u>52.49</u>
<i>PointNSP-m (ours)</i>	Autoregressive	66.98	56.05	54.01	53.76	53.12	50.09	58.04	52.30

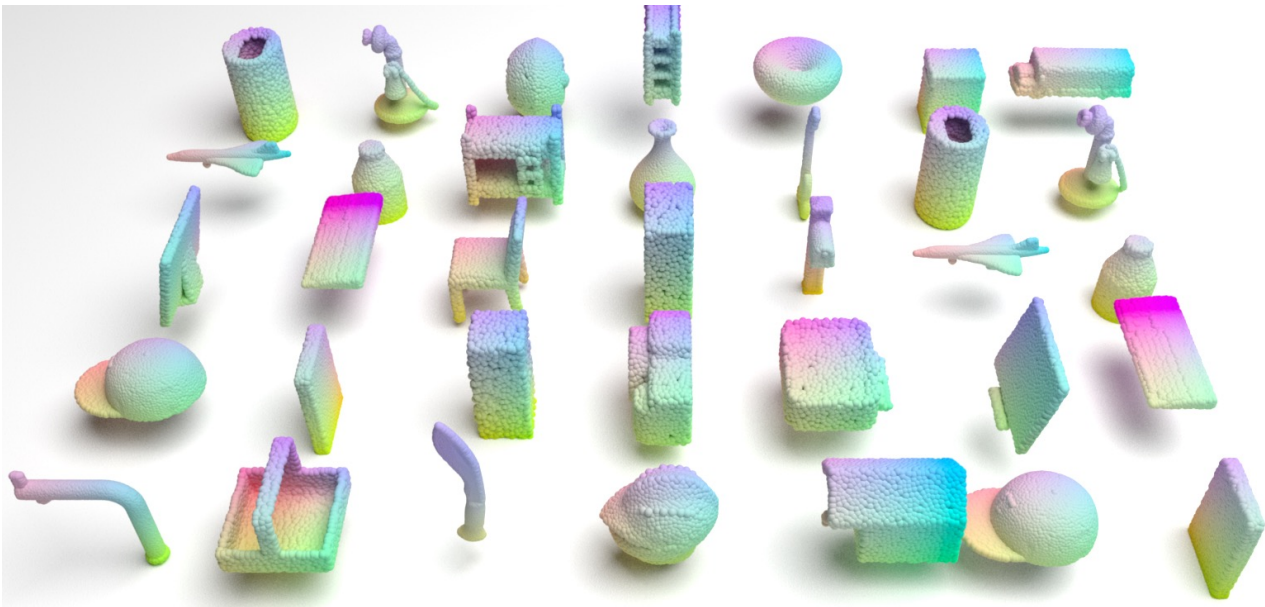


Figure S3. Generated shapes from the *PointNSP* model trained on ShapeNet’s other categories.

models. In contrast, PUDM [45] directly utilizes conditional diffusion models, treating sparse point clouds as input conditions for generating denser outputs. In this work, our generative model, *PointNSP*, incorporates upsampling networks in both two training stages, making it well-suited for

enhancing downstream point cloud upsampling tasks.

12. Limitations & Broader Impact

PointNSP does not exhibit major limitations, though a primary challenge lies in learning high-quality multi-scale



Figure S4. Generated shapes from the *PointNSP* model trained on ShapeNet’s other categories.

codebook embeddings for 3D point cloud representations, particularly in avoiding codebook collapse. Several promising directions arise for future work. One avenue is scaling generation toward ultra-dense point clouds (e.g., 10k–100k points), which could subsequently be converted into high-fidelity meshes. Another is enabling fine-grained control over local geometric structures, a capability crucial for practical deployment. Although this work does not present immediate societal risks, potential misuse for generating harmful 3D content warrants careful consideration by the broader community. From a research standpoint, *PointNSP* represents a significant contribution to both the generative modeling and 3D point cloud communities.



Figure S5. Generated single-class shapes from the *PointNSP* model trained on ShapeNet's other categories.

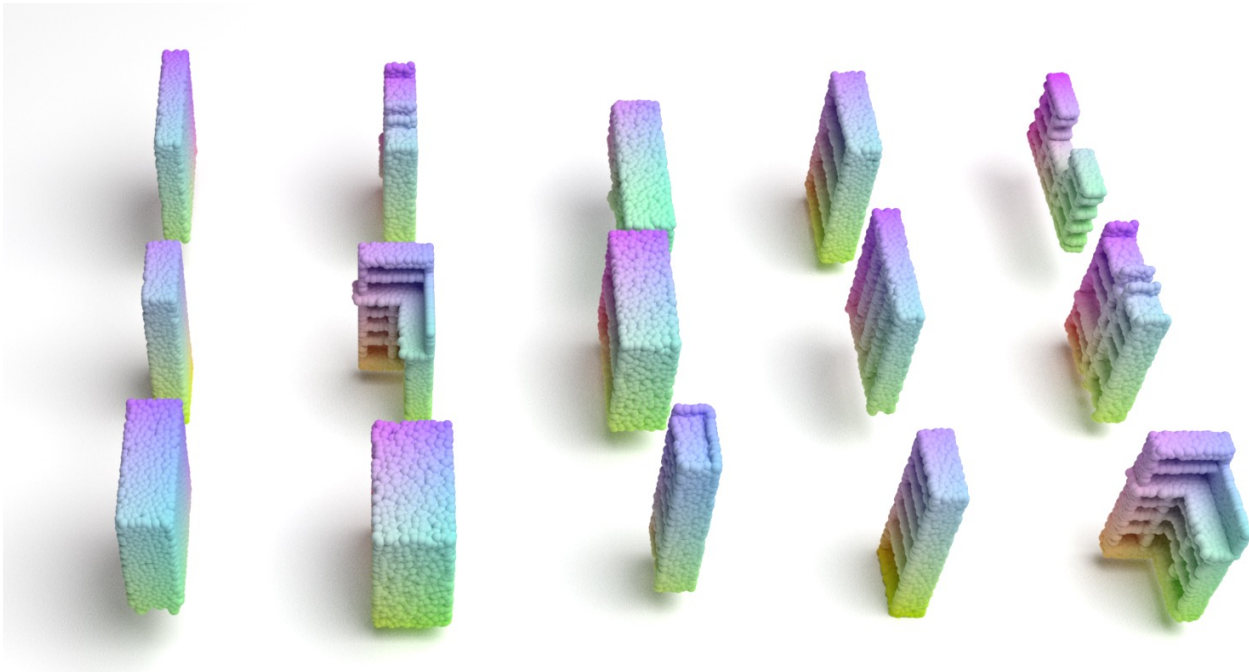


Figure S6. Generated single-class shapes from the *PointNSP* model trained on ShapeNet's other categories.

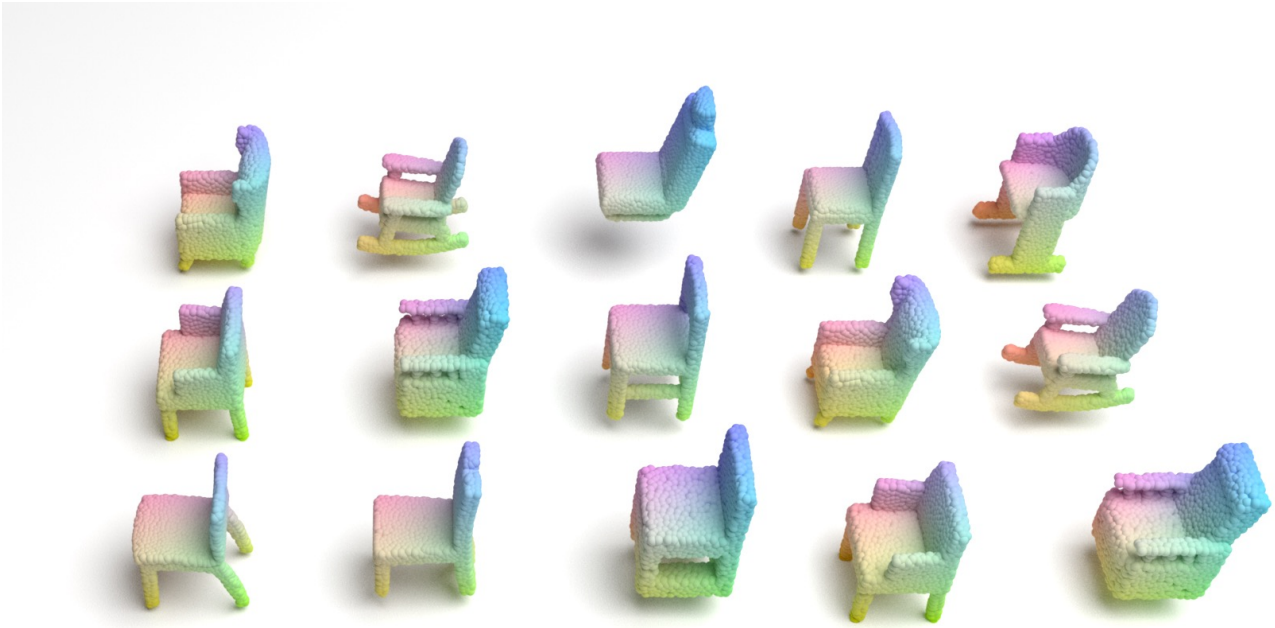


Figure S7. Generated single-class shapes from the *PointNSP* model trained on ShapeNet's other categories.

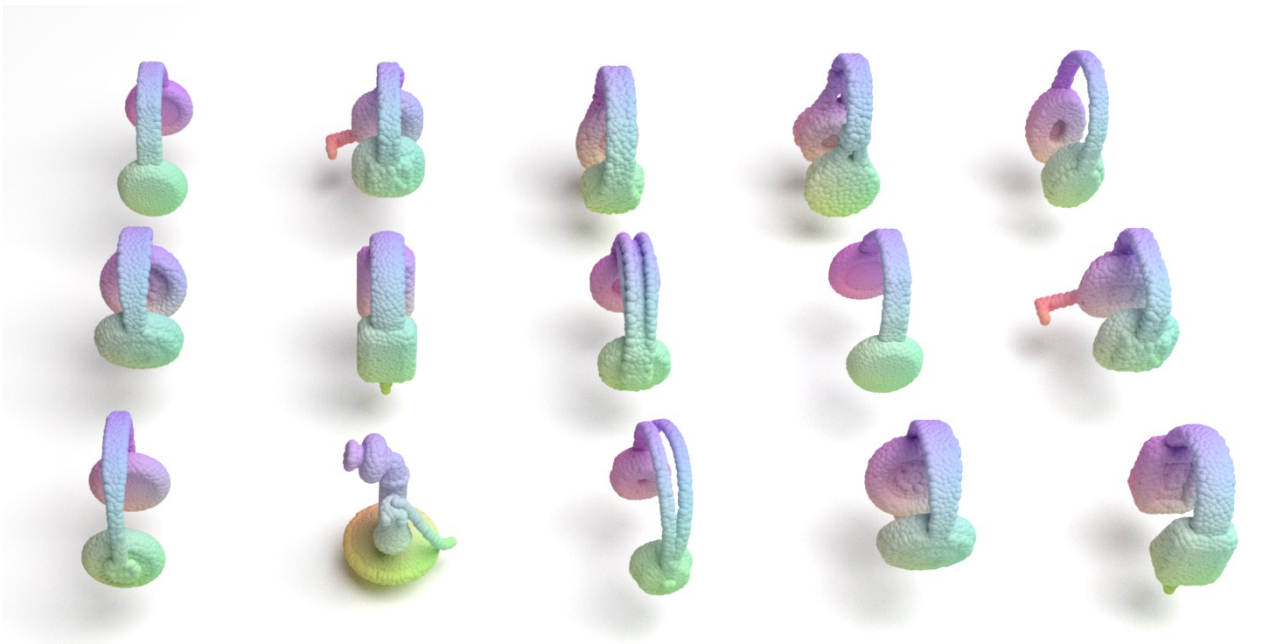


Figure S8. Generated single-class shapes from the *PointNSP* model trained on ShapeNet's other categories.

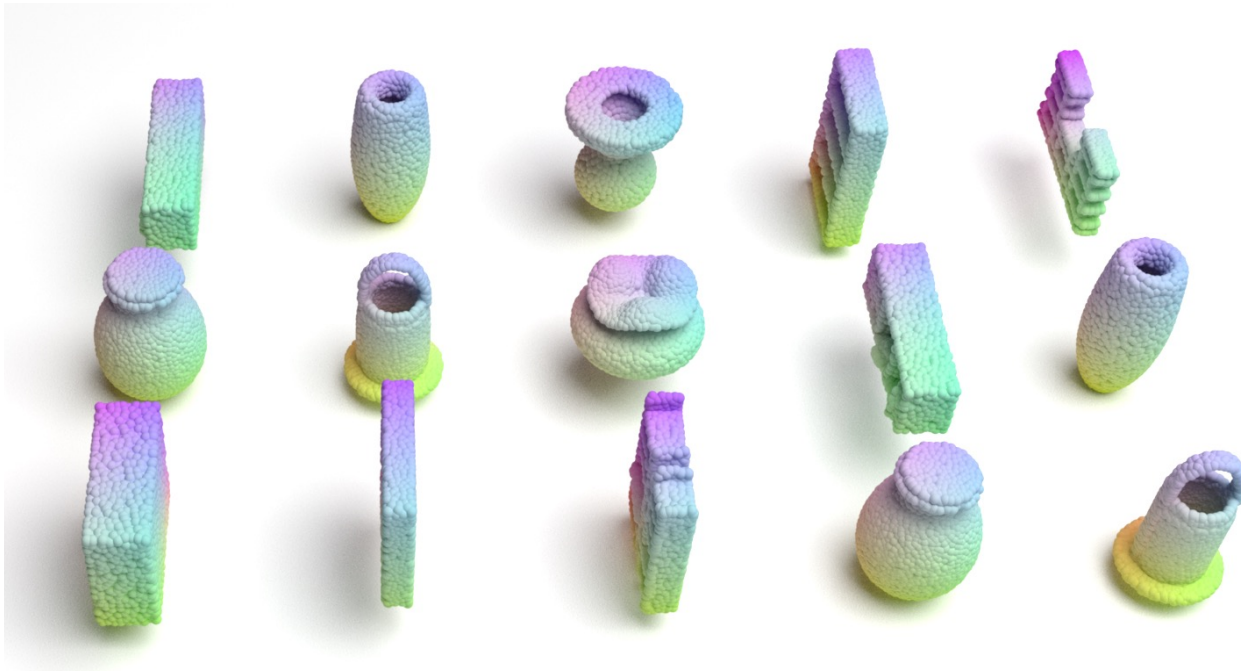


Figure S9. Generated single-class shapes from the *PointNSP* model trained on ShapeNet's other categories.

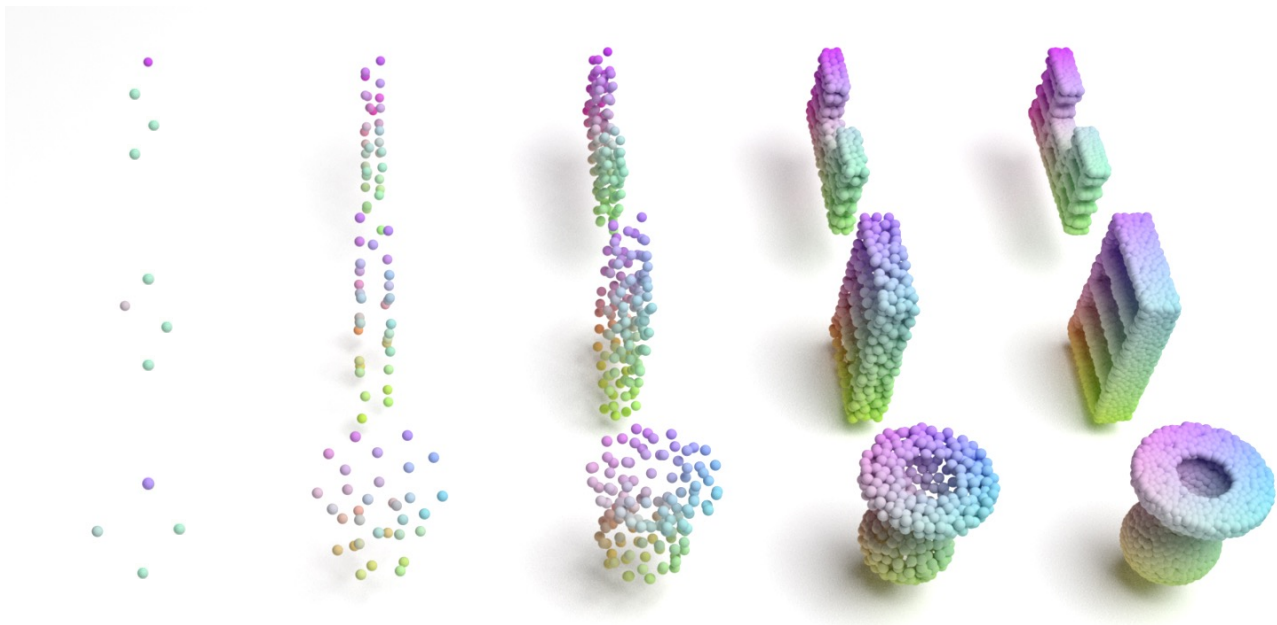


Figure S10. Illustration of multi-scale point cloud generation from the *PointNSP* model.

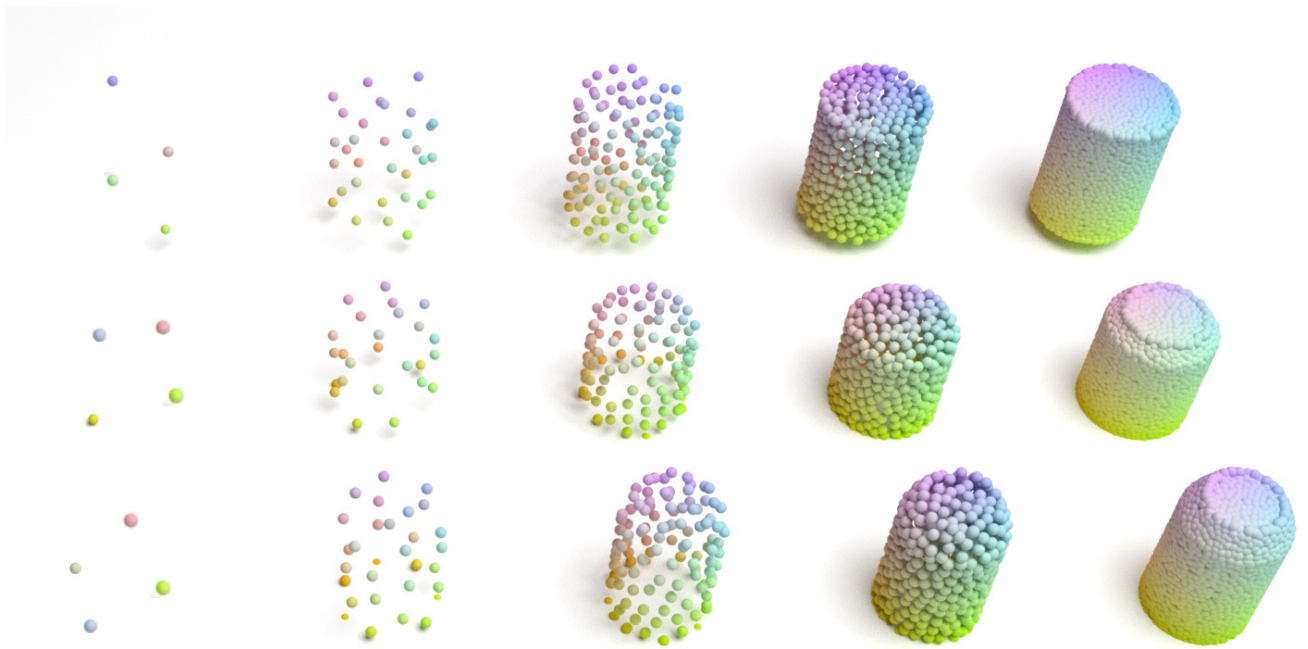


Figure S11. Illustration of multi-scale point cloud generation from the *PointNSP* model.

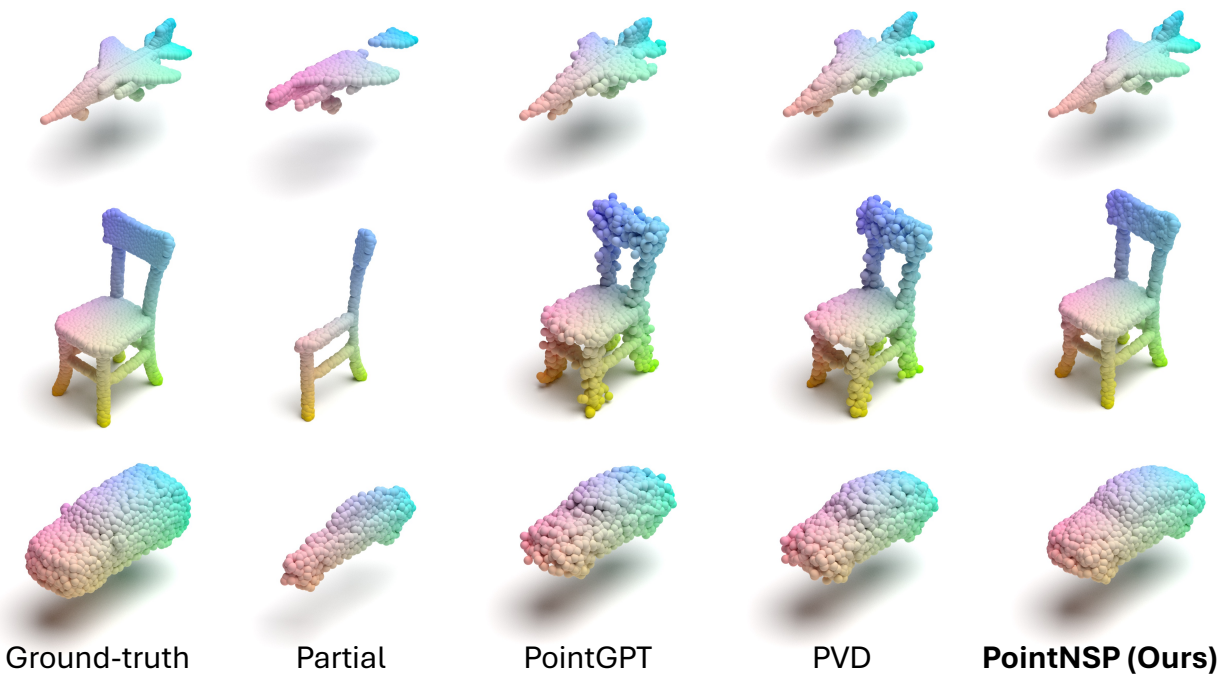


Figure S12. Visualizations of more point cloud completion results.

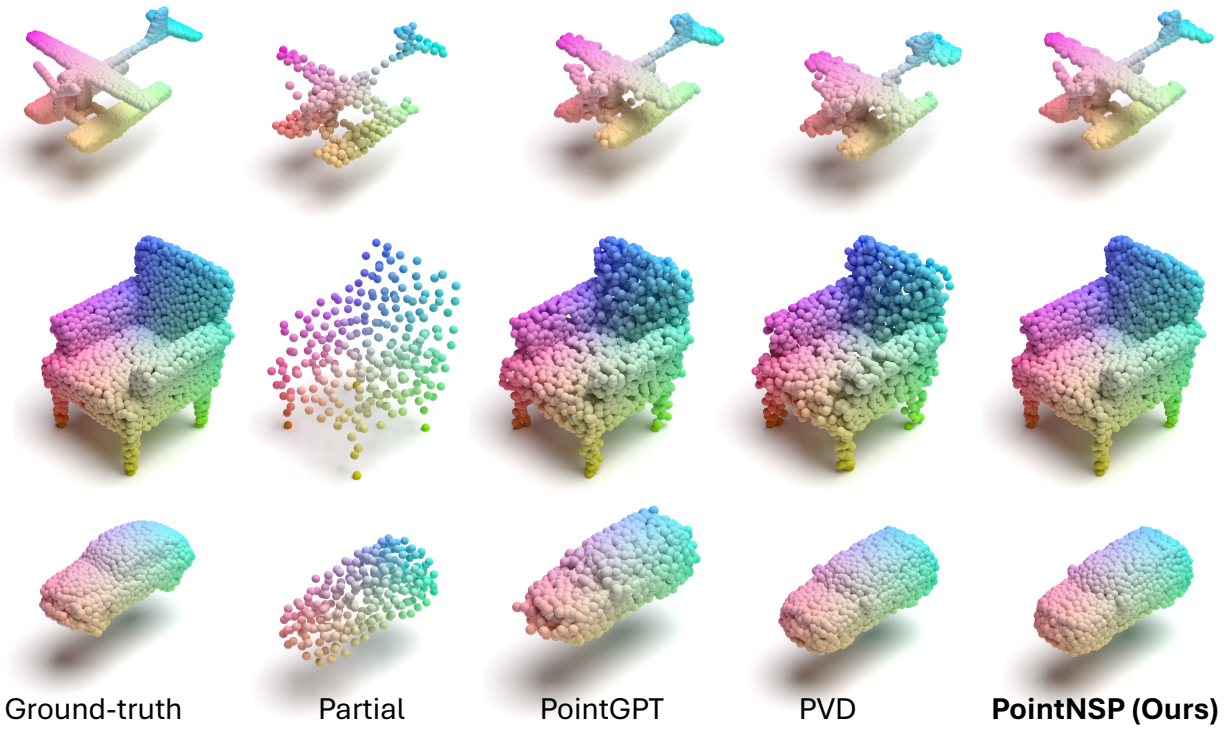


Figure S13. Visualizations of more point cloud upsampling results.